PLOS BIOLOGY

METHODS AND RESOURCES

Network modeling of dynamic brain interactions predicts emergence of neural information that supports human cognitive behavior

Ravi D. Mill[1]*, Julia L. Hamilton[1], Emily C. Winfield[1], Nicole Lalta[1], Richard H. Chen[1,2], Michael W. Cole[1]

1 Center for Molecular and Behavioral Neuroscience, Rutgers University, Newark, New Jersey, United States of America, **2** Behavioral and Neural Sciences Graduate Program, Rutgers University, Newark, New Jersey, United States of America

* rdm146@rutgers.edu

Check for updates

OPEN ACCESS

Citation: Mill RD, Hamilton JL, Winfield EC, Lalta N, Chen RH, Cole MW (2022) Network modeling of dynamic brain interactions predicts emergence of neural information that supports human cognitive behavior. PLoS Biol 20(8): e3001686. https://doi.org/10.1371/journal.pbio.3001686

Academic Editor: Claus C. Hilgetag, University Medical Center Hamburg-Eppendorf: Universitatsklinikum Hamburg-Eppendorf, GERMANY

Received: October 1, 2021

Accepted: May 24, 2022

Published: August 18, 2022

Copyright: © 2022 Mill et al. This is an open access article distributed under the terms of the Creative Commons Attribution License, which permits unrestricted use, distribution, and reproduction in any medium, provided the original author and source are credited.

Data Availability Statement: Raw and preprocessed EEG data used in the present report are accessible via the Open Science Foundation (https://osf.io/mw4k3/). The individual quantitative observations (i.e. information decoding timecourses for each subject over time) for the key Results figures (Figs 4, 5, 6 and 7) are also accessible from the same repository (subdirectory: 'Results_figures_data'). The critical analysis code used to 1) calculate restFC via the MVAR approach,

Abstract

How cognitive task behavior is generated by brain network interactions is a central question in neuroscience. Answering this question calls for the development of novel analysis tools that can firstly capture neural signatures of task information with high spatial and temporal precision (the "where and when") and then allow for empirical testing of alternative network models of brain function that link information to behavior (the "how"). We outline a novel network modeling approach suited to this purpose that is applied to noninvasive functional neuroimaging data in humans. We first dynamically decoded the spatiotemporal signatures of task information in the human brain by combining MRI-individualized source electroencephalography (EEG) with multivariate pattern analysis (MVPA). A newly developed network modeling approach—dynamic activity flow modeling—then simulated the flow of task-evoked activity over more causally interpretable (relative to standard functional connectivity [FC] approaches) resting-state functional connections (dynamic, lagged, direct, and directional). We demonstrate the utility of this modeling approach by applying it to elucidate network processes underlying sensory–motor information flow in the brain, revealing accurate predictions of empirical response information dynamics underlying behavior. Extending the model toward simulating network lesions suggested a role for the cognitive control networks (CCNs) as primary drivers of response information flow, transitioning from early dorsal attention network-dominated sensory-to-response transformation to later collaborative CCN engagement during response selection. These results demonstrate the utility of the dynamic activity flow modeling approach in identifying the generative network processes underlying neurocognitive phenomena.

Introduction

Clarifying the spatial and temporal signatures underlying cognitive task information is critical to understanding the brain. Toward this aim, multivariate pattern analysis (MVPA)

and 2) generate task activation predictions via dynamic activity flow modeling are available here https://github.com/ColeLab/DynamicSensoryMotorEGI_release.

Funding: The authors acknowledge support by the US National Institutes of Health under awards R01 AG055556 and R01 MH109520 to MWC. EEG equipment used in this report was supplied by the US National Science Foundation (award BCS-1530930). The content is solely the responsibility of the authors and does not necessarily represent the official views of any of the funding agencies. The funders had no role in study design, data collection and analysis, decision to publish, or preparation of the manuscript.

Competing interests: The authors have declared that no competing interests exist.

Abbreviations: ANN, artificial neural network; CCN, cognitive control network; EEG, electroencephalography; EOG, electrooculogram; ERP, event-related potential; FC, functional connectivity; FDR, false discovery rate; FEM, finite element modeling; fMRI, functional MRI; ICA, independent component analysis; IIR, infinite impulse response; IRB, Institutional Review Board; HC-GSN, HydroCel Geodesic Sensor Net; LCMV, linearly constrained minimum variance approach; MEG, magnetoencephalography; MNE, minimum norm estimate; MSE, mean squared error; MVAR, multivariate autoregression; MVPA, multivariate pattern analysis; nPCs, number of predictor principal components; PCA, principal component analysis; resfFC, resting-state functional connectivity; RUBIC, Rutgers University Brain Imaging Center; SVM, support vector machine; TACS, transcranial alternating current stimulation; TMS, transcranial magnetic stimulation.

approaches have enabled decoding of different types of task information (e.g., sensory information in presented stimuli or response information underlying behavior) from evoked neural activation patterns [1–3]. Prior research has shown these multivariate approaches to be more sensitive in relating neural activation measures to cognitive and behavioral variables of functional interest than earlier univariate approaches (e.g., single-cell spike rates, event-related potentials (ERPs) and functional MRI (fMRI) general linear model activations; [4–7]). These empirical observations underpin a shift in theoretical focus from localization of function to mapping distributed functionality at the neural population level [8].

Decoding methods applied to animal electrophysiological data have revealed that task-related information is highly distributed throughout cortex, such that many forms of task information can be decoded from multiple recorded brain regions [9–13]. However, a degree of functional specialization has been demonstrated by scrutiny of temporal decoding characteristics, such as sensory information onsetting earliest in visual regions [13,14]. Functional neuroimaging studies have interrogated the neural basis of task information noninvasively in humans, with fMRI highlighting a central role for large-scale spatial interactions between sensory/motor content networks and higher-order cognitive control networks (CCNs, i.e., dorsal attention, frontoparietal, and cingulo-opercular networks; [15–17]). Recent applications of MVPA decoding in scalp/sensor-level electroencephalography/magnetoencephalography (EEG/MEG) data have hinted at complex information dynamics, involving short timescale transitions between distinct whole-brain representations as sensory information is translated into a behavioral response [18–20].

Critically, all of the aforementioned recording methods have their respective limitations: invasive electrophysiology has high spatial resolution, high temporal resolution, but only partial spatial coverage; fMRI has high spatial resolution, low temporal resolution, and full spatial coverage; sensor-level EEG/MEG has low spatial resolution, high temporal resolution and full spatial coverage. These methodological limitations have impeded a comprehensive spatiotemporal description of both spatially "where" and temporally "when" task information is decodable from brain activity. Moreover, the spatiotemporal coding schemes by which CCNs impact on task information and resulting behavior remain unresolved, as this would require analytic approaches that optimally balance spatial resolution, temporal resolution, and whole-brain coverage.

Consequent to this lack of descriptive insight is an even greater dearth of understanding into the network computations (the "how") underpinning task information. This deeper insight relies on the formalization of candidate models of how representations are computed (and transferred) across the brain, which are lacking in MVPA decoding approaches per se [21]. To this end, it is likely that connectivity between neural entities plays a formative role in the computations that give rise to decodable information at specific spatial locations and temporal epochs [22]. This follows from classical demonstrations of connectivity at the cellular level weighting the flow of action potentials via structural connectivity and Hebbian synaptic strength processes [23,24]. Such small-scale connectivity is theorized to coordinate the formation of "cell assemblies" representing task information at the population level [8,25]. A role for human neuroimaging-assessed functional connectivity (FC) as a large-scale aggregate of synaptic strengths has been hypothesized [26,27] and supported by evidence of long-term learning- and use-driven changes to FC [28,29]. While this supports a role for repeated task coactivation in molding connectivity, a reciprocal influence is also anticipated by Hebbian theory: the intrinsic network architecture estimated via resting-state functional connectivity (restFC) should determine the likelihood of activity propagating between brain regions. Supporting evidence comes from recent "activity flow" models linking the emergence of task activations to communication pathways indexed by restFC. The observed accuracy in predicting

empirical brain activations across a variety of cognitive tasks [16,30] and in predicting dysfunctional activations and behavior in Alzheimer disease [31] substantiates the relevance of restFC in capturing the intrinsic network architecture that generates cognitively relevant phenomena [32].

However, these previous network models focused exclusively on predicting the spatial signatures of task activations and overlooked accompanying dynamics. This is in part due to their sole application in fMRI, which has well-known temporal limitations. We therefore developed a new dynamic version of activity flow modeling suited to higher temporal resolution EEG data (see Fig 1 for a task schematic and Fig 2 for our source modeling pipeline), so as to elucidate the dynamic neural computations underlying cognition. Importantly, we could not simply apply previous activity flow models—using contemporaneous brain activity in one region to predict contemporaneous activity in an independent brain region—to EEG data. This was due to well-known instantaneous field spread artifacts in EEG (and MEG) data [33,34], which could result in analytic circularity if a to-be-predicted region leaked some of its signal into other regions used as predictors. A substantial innovation was necessary to overcome this limitation: updating activity flow modeling to use past activity to predict future activity. Given that it is impossible for brain activity to propagate back in time (a fundamental principle of causality and the direction of time), this considerably reduced the possibility of analytic circularity. As described in the Methods section, we implemented further rigorous steps during preprocessing (use of causal temporal filters), source reconstruction (use of dense

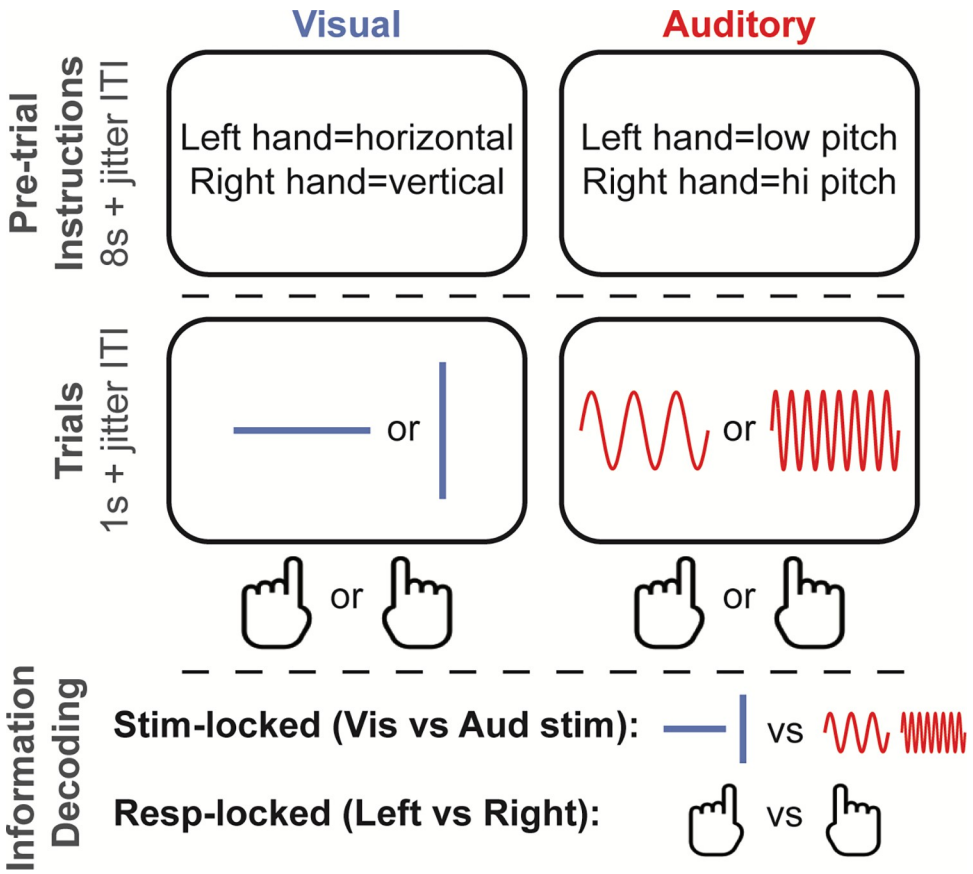

Fig 1. Task design. Depicted is one trial from each sensory block condition (10 trials per block, 12 blocks per participants session) and the types of decodable task information.

https://doi.org/10.1371/journal.pbio.3001686.g001

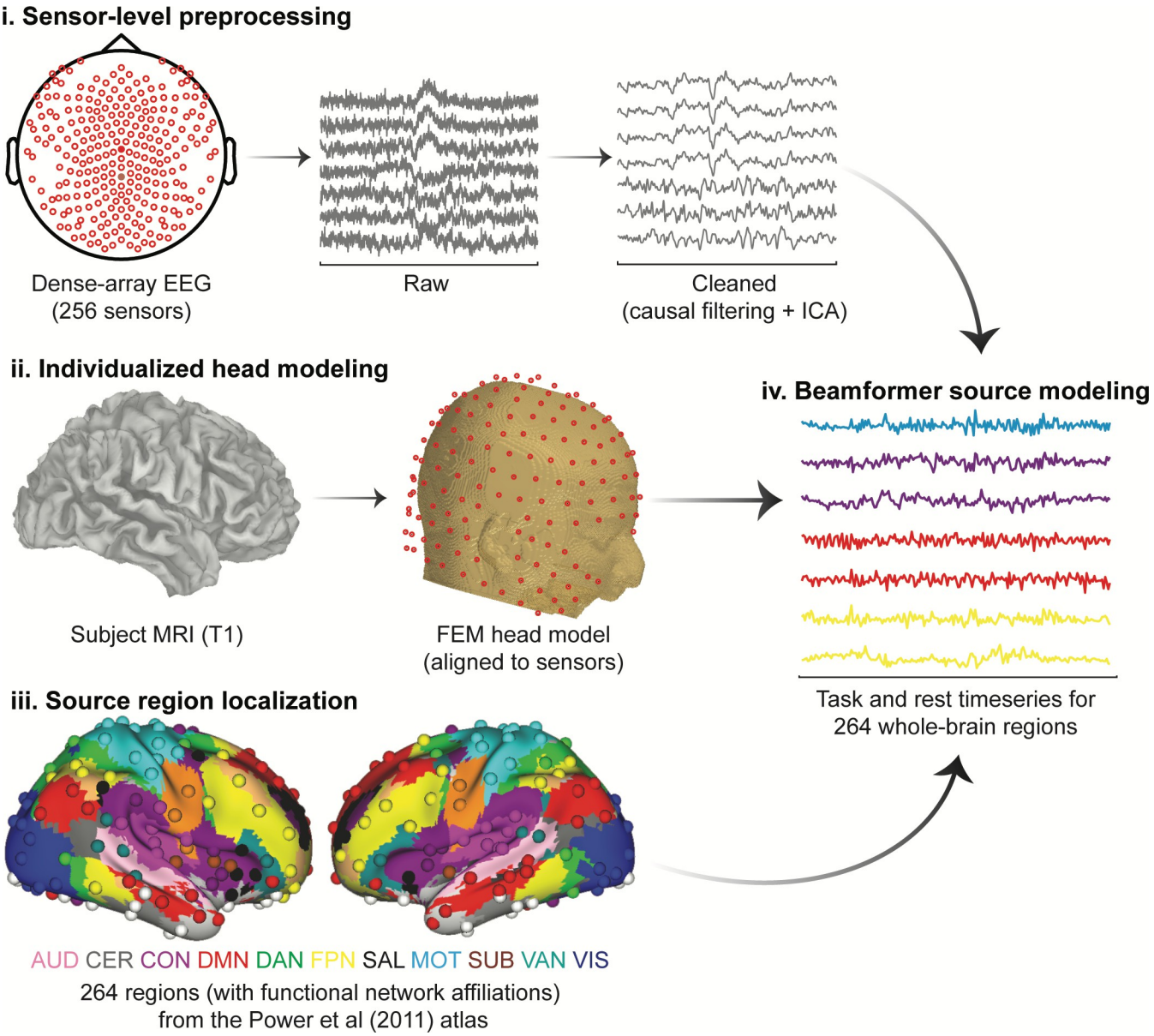

Fig 2. EEG preprocessing and source modeling pipeline. Applying this pipeline separately to task and resting-state EEG data reconstructed their respective activation time series. Colored text in panel (iii) provides functional network affiliations for correspondingly colored regions localized from the Power functional atlas: AUD, auditory; CER, cerebellar; CON, cingulo-opercular; DMN, default mode; DAN, dorsal attention; FPN, frontoparietal; SAL, salience; MOT, motor; SUB, subcortical; VAN, ventral attention; VIS, visual. See Methods for full details. EEG, electroencephalography; FEM, finite element modeling; ICA, independent component analysis.

https://doi.org/10.1371/journal.pbio.3001686.g002

array EEG, individual structural MRIs, and beamformer source modeling) and dynamic activity flow modeling (regressing out to-be-predicted region time series from all predictors prior to running all modeling analyses) to conclusively eliminate the risk of field spread and associated circularity.

An added benefit of our novel network modeling approach was that the empirical restFC weights parameterizing the models were derived from multivariate autoregression (MVAR) applied in the resting state (see Fig 3A). This captured dynamic, lagged, direct, and directional connectivity between regions, rendering the models more causally valid than alternative approaches to estimating restFC (e.g., Pearson correlation; see Methods for how these features

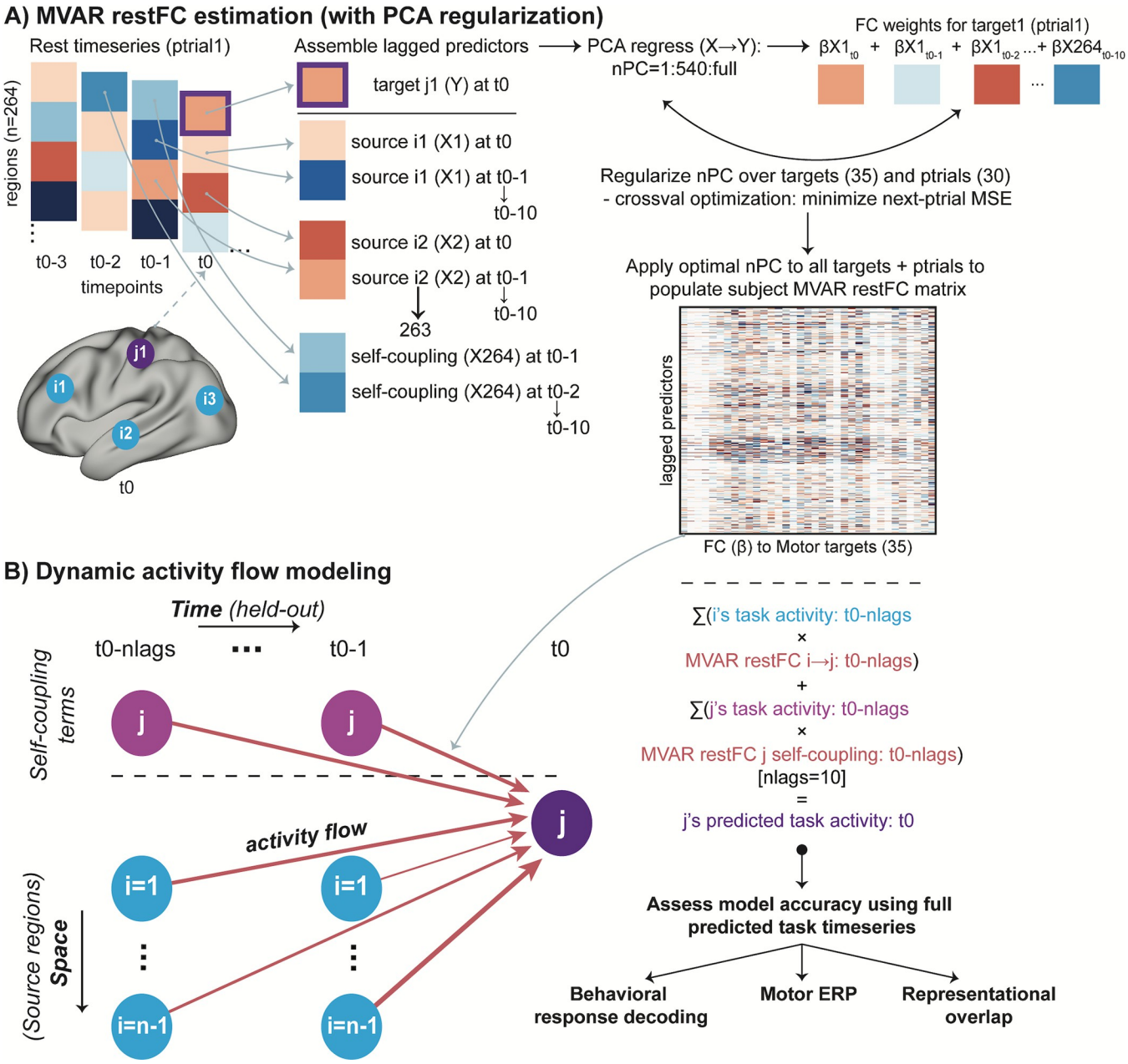

Fig 3. Approach to restFC estimation (via MVAR) and dynamic activity flow modeling. (A) Estimation of MVAR restFC. Note that for demonstration purposes the schematic uses just 4 regions (1 Motor network target j1, and 3 predictor sources i1-3), whereas the full procedure iterated over 35 Motor targets and included all other 263 regions as sources. Lagged FC weights (β) from source regions and self-coupling terms to each Motor network region were calculated after regularizing the nPCs. This was achieved via cross-validated minimization of the MSE of the MVAR-predicted rest time series for held-out ptrials. **(B)** The lagged MVAR restFC weights were then combined with the lagged task activation time series to predict future Motor task activations via dynamic activity flow modeling. Iterating over all to-be-predicted Motor targets [35], ptrials (approximately 30), and trial time points (−0.45 to 0.45 s around response commission) populated the full predicted Motor task activation matrix. This predicted matrix was the basis of subsequent response information decoding (dynamic MVPA), motor ERP, and representational overlap analyses that assessed model accuracy. ERP, event-related potential; FC, functional connectivity; MSE, mean squared error; MVAR, multivariate autoregression; nPCs, number of principal components; PCA, principal component analysis; ptrial, pseudo-trial; restFC, resting-state functional connectivity.

https://doi.org/10.1371/journal.pbio.3001686.g003

were derived from the causal inference/connectivity literatures). These innovations were necessary to achieve the desired prediction outcome: moment-to-moment fluctuations in future task information. This aligns activity flow modeling with the fully dynamic simulations of task

information output by certain artificial neural network (ANN) models [35–37]), with the added benefits of empirical estimation of connectivity weights (versus random initiation and optimization in ANNs; [38]) and direct assessment of whether the engineered representations overlap veridically with those in the brain [39].

In the present report, we sought to demonstrate the utility of this novel dynamic activity flow modeling approach via example application in clarifying the flow of cognitive task information in a simple sensory–motor categorization task (Fig 1). We first identified different forms of task information (sensory and response information; see Fig 1) using a combination of anatomically individualized EEG source modeling and dynamic MVPA, which richly described large-scale spatial and temporal information signatures (Fig 2).

After describing these signatures, we simulated their emergence using dynamic activity flow modeling (Fig 3). We first tested whether the full model can successfully predict future response information dynamics of the brain, thereby evidencing the cognitive and behavioral relevance of restFC as a large-scale analogue of synaptic strength processes governing neural information flow. Our ability to successfully model response information using connectivity weights that were entirely held-out from the task would also provide support for restFC in capturing the brain's intrinsic (i.e., state-general) functional network architecture. Second, we extended the modeling framework to construct alternative network models (derived via simulated lesions to particular networks) to test the hypothesis that information flowing from the CCNs specifically (i.e., over and above the other functional networks) to the Motor network is central to producing behavior. We also sought to clarify the dynamic network computations used to fulfill this goal, so as to preliminarily highlight the functional utility of dynamic activity flow modeling in linking large-scale networks to more refined neurocognitive roles.

Results

Behavioral task performance

All participants were able to perform the task, with accuracy significantly above chance for both the visual (mean = 92.5%, Wilcoxon z = 4.94, $p < 0.001$) and auditory (mean = 91.5%, z = 4.94, $p < 0.001$) conditions. Accuracy did not significantly differ between these 2 conditions (paired Wilcoxon z = 0.27, $p = 0.789$). The average reaction time (RT) for the visual and auditory conditions was 464.6 s and 527.9 s, respectively, with RT significantly slower in the auditory condition (z = 4.66, $p < 0.001$). This RT difference motivated a primary focus on response-locked rather than stimulus-locked trial data in subsequent analyses.

Source modeling improves detection of cognitive task information

We compared peak information decodability for our approach that combined individualized source modeling and dynamic MVPA, with the more commonly used sensor-level dynamic MVPA approach. Time point–by–time point behavioral response information (correct left- versus right-handed responding) was decoded separately using all source regions (SourceAll) and all scalp sensors (SensorAll) as features. Visual inspection of the group response information time courses (Fig 4) revealed multiple significantly decodable time points for both feature sets, with onset prior to commission of the response. This morphology is consistent with previous response decoding of EEG [18] and invasive electrophysiological [13] data.

Critically, peak response information decodability was visibly higher for the source-modeled approach (Fig 4). This was formalized statistically by extracting peaks from each participant's SensorAll and SourceAll decoding time courses, and contrasting them via paired Wilcoxon tests. The SourceAll decoding peak was significantly higher than the SensorAll peak across variation in how time-to-peaks were defined: (i) from the SensorAll group time-to-peak (0.025 s; 3.8% peak

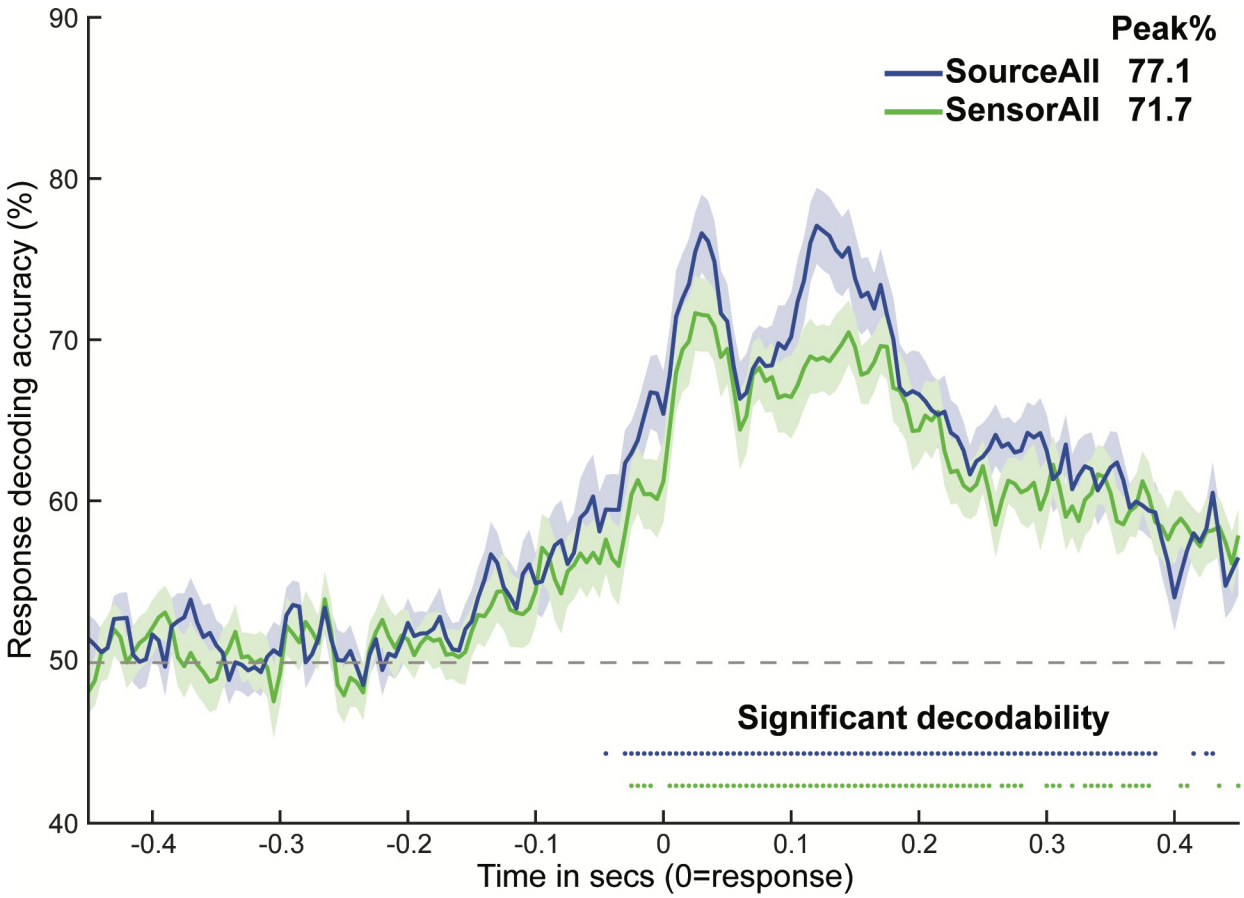

Fig 4. Detection of behavioral response information is improved for source versus sensor feature sets. Group-averaged response decoding time courses for the SourceAll and SensorAll sets, with shaded patches reflecting the standard error of the mean across time points. Colored dots represent time points with significantly decodable information, as assessed by Wilcoxon sign rank tests against 50% classification accuracy ($p < 0.05$, Bonferroni corrected). The legend in the top right provides the peak decoding accuracy for each time course. Subject-level data underlying this figure are accessible via the public data repository (https://osf.io/mw4k3, subdirectory: Results_figures_data/Figure4).

https://doi.org/10.1371/journal.pbio.3001686.g004

change; z = 2.47, $p = 0.014$); (ii) from the SourceAll group time-to-peak (0.120 s; 8.4% peak change; z = 3.57, $p < 0.001$); and (iii) from the peak of each individual participant's decoding time course (unbiased by the group results; 4.8% peak change; z = 3.59, $p < 0.001$). Peak decodability of sensory information (visual versus auditory stimulus condition) was also numerically higher for SourceAll compared to SensorAll features (panel A of Fig A in S1 Text). Hence, combining source modeling with dynamic MVPA significantly improved detection of response information. This might have arisen from improvements in signal-to-noise introduced by beamformer source modeling [40], and opposes prior suggestions that beamforming leads to overarching cancelation of the underlying neural activations [41,42]. These results extended our critical requirement for subsequent analyses—that spatially distinct regions were localized accurately—by demonstrating that such source localization can actually improve overall decodability.

Network decoding reveals prominent roles of Motor network and CCNs in representing behavioral response information

We then applied our source-modeled dynamic MVPA approach to decode spatial and temporal signatures of response information from each of the 11 major functional networks [43],

treating within-network regions as features (see Methods). To clarify, we focused on the network rather than region level as a principled decision following prior demonstrations of the precision afforded by EEG source modeling (approximately 3- to 10-mm cortical localization error; [44–46]). The lower end of this range questions an alternative "searchlight" approach previously applied to fMRI data, which decodes information using within-region voxels/vertices (typically of approximately <3 mm resolution) as features. We hence focused on the network level, which aligned with our a priori interest in making functional inferences at this level. Despite this spatial scale being somewhat coarse (compared to invasive animal methods), it is worthwhile reiterating that this permits a degree of spatial insight that sensor-level EEG/MEG analyses are singularly incapable of.

The network decoding results are depicted in Fig 5. Consistent with the morphology of the SourceAll response decoding time course (Fig 4), we again observed 2 decoding peaks across networks. In the Supporting information (S1 Text), we link this 2-peak morphology to sequential motor preparation and motor execution/feedback processes, both via stimulus-locked response decoding (Fig C in S1 Text, panels A and B) and via a temporal generalization analysis that revealed distinct multivariate codes for each peak (Fig C in S1 Text, panel C).

Response information was broadly decodable across networks, consistent with prior findings from primate electrophysiology [9,13] and rodent optical imaging [10]. However, despite the visible similarity of the network time courses, examination of time course features revealed content-appropriate specialization: response information onset earliest and peaked strongest in the Motor network. Similar content-appropriate specialization was observed when decoding stimulus categories within each sensory modality, with visual stimulus information (horizontal versus vertical lines) peaking in the Visual network and auditory stimulus information (low versus high pitch sounds) peaking in the Auditory network (Fig B in S1 Text).

Prominent response decodability was also observed in the CCNs, all 3 of which yielded the highest response information peaks after the Motor network. We statistically formalized these between-network effects by contrasting decoding time course peaks extracted from individual participants (see Methods). We extracted subject-level peaks separately for peak 1 (motor preparation, Fig 5B) and peak 2 (motor execution/feedback, Fig 5D), from the respective cross-network group peak time points within these windows (0.03 s and 0.125 s). Motor network activity was decoded significantly higher relative to other networks across both peak 1 (Fig 5C) and peak 2 (Fig 5E). Interestingly, whereas Visual network activity was prominently decoded during peak 1 (see network ranking in Fig 5B), it was much less involved in peak 2 (Fig 5D). One possibility is that this earlier period reflects motor preparation operations that translate sensory into response information, whereas the later peak 2 period may reflect purer motor representations underlying response execution and feedback, consistent with prior animal [11,47] and human motor ERP [48] research.

The transition from peak 1 to peak 2 also charted an interesting differentiation in the engagement of the CCNs. The DAN was more prominently involved in the motor preparation peak 1 and differed significantly from both the CON and FPN (Fig 5B). This profile of preferential DAN engagement was also observed when sensory information was more directly decoded from the stimulus-locked data (panel B of Fig A in S1 Text), suggesting that similar sensory-related computations might be occurring at peak 1 in the response time course. However, the later peak 2 elicited a different network profile: information was higher for all 3 CCNs relative to the other networks but was not reliably differentiated between them (even at an uncorrected threshold of $p < 0.05$, Fig 5E).

Overall, the network decoding results highlight the utility of decoding information from neuroimaging data that is well resolved in both the spatial and temporal domains, as was uniquely enabled by our combination of source EEG and dynamic MVPA. Beyond recovering

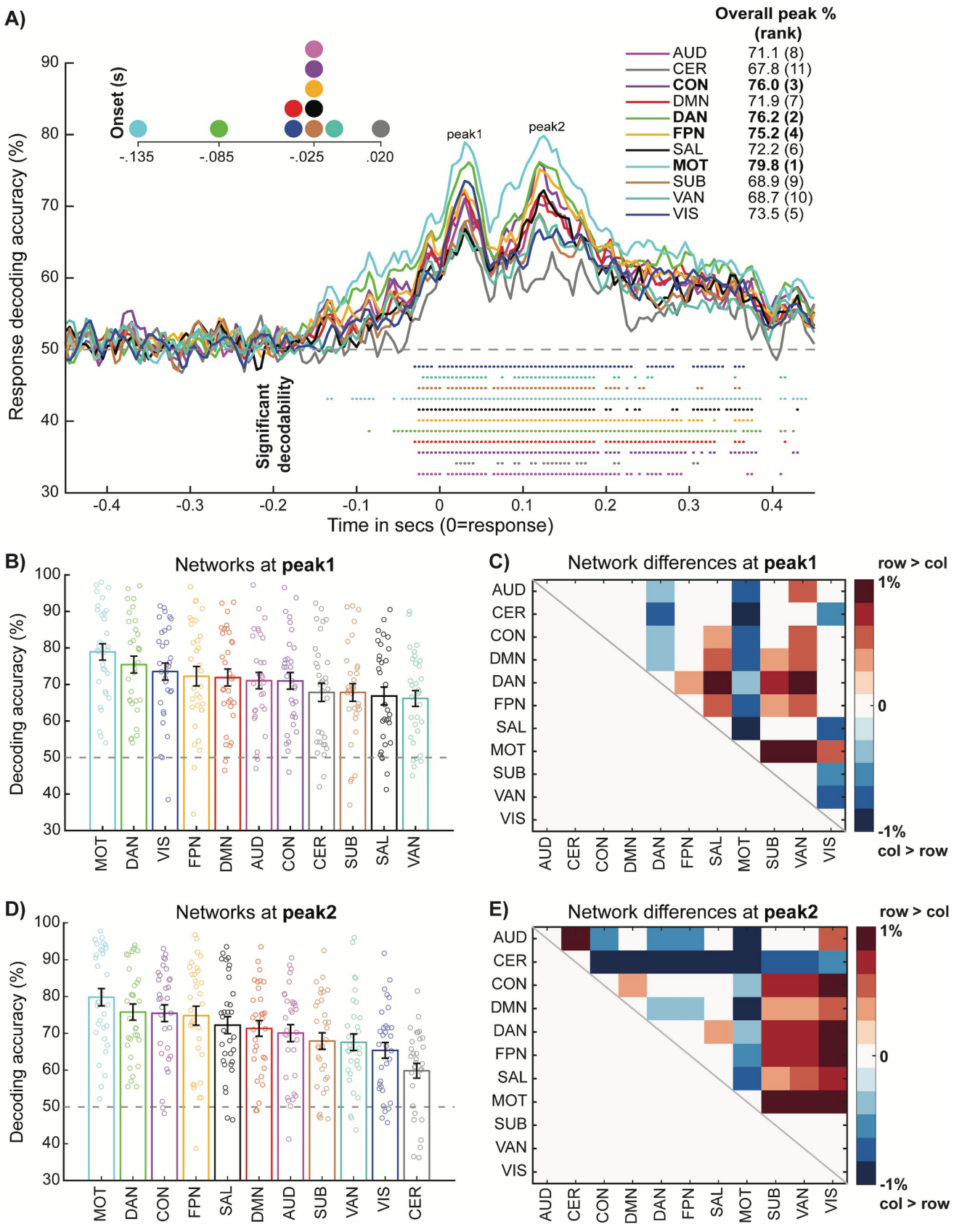
A)
Overall peak %
(rank)
AUD 71.1 (8)
CER 67.8 (11)
CON 76.0 (3)
DMN 71.9 (7)
DAN 76.2 (2)
FPN 75.2 (4)
SAL 72.2 (6)
MOT 79.8 (1)
SUB 68.9 (9)
VAN 68.7 (10)
VIS 73.5 (5)
Onset (s)
-.135
-.085
-.025
.020
peak1
peak2
Response decoding accuracy (%)
Significant decodability
Time in secs (0=response)
B)
Networks at peak1
Decoding accuracy (%)
MOT DAN VIS FPN DMN AUD CON CER SUB SAL VAN
C)
Network differences at peak1
row > col
col > row
D)
Networks at peak2
MOT DAN CON FPN SAL DMN AUD SUB VAN VIS CER
E)
Network differences at peak2

Fig 5. Network decoding of behavioral response information reveals prominent roles for Motor network and CCNs. (A) Group decoding time courses color-coded by network affiliation. Colored dots represent significantly decodable time points for each network ($p < 0.05$ via Wilcoxon sign rank against 50% chance, Bonferroni corrected) and the legend in the top right provides peak decoding accuracies for each network. A magnified plot of the onset of the first significant time point for each network is provided in the top left. **(B)** Response decoding accuracy ranked across networks at peak 1 (0.03 s). Each bar represents the mean and standard error for each network, with individual participant data points also overlaid. **(C)** Matrix capturing the significance of cross-network differences in decoding accuracy at peak 1. Plotted is the pairwise difference in mean decoding accuracy, thresholded via paired Wilcoxon tests ($p < 0.05$, FDR corrected). Positive values denote significantly higher decoding accuracy for the row network > the column network and vice versa for the negative values. **(D)** and **(E)** follow the same conventions as (C) and (D), respectively, albeit focusing on peak 2 (0.125 s). Subject-level data underlying this figure are accessible via the public data repository (https://osf.io/mw4k3, subdirectory: Results_figures_data/Figure5). CCN, cognitive control network; FDR, false discovery rate.

https://doi.org/10.1371/journal.pbio.3001686.g005

the content-appropriate specialization of the Motor network for response information, this approach led to a segregation of dynamic CCN profiles: from preferential engagement of the DAN during translation of sensory to response information at peak 1, to more collaborative engagement of all 3 CCNs to generate purer response representations at peak 2. In the Supporting information (Fig D in S1 Text), we demonstrate that the pattern of network decoding results is highly similar when using an alternative approach that confines the decoding to more "unique" signals within each network.

Dynamic activity flow modeling predicts future response information dynamics

The preceding network decoding results described which spatial networks prominently represent response information ("where") and their accompanying temporal profiles ("when"). We next sought insight into "how" these representations emerge computationally from dynamic network interactions in the brain. We treated this simplified sensory–motor task scenario as a testbed for our novel network modeling approach (dynamic activity flow) and used it to predict future response information dynamics from past task activations flowing over communication pathways parameterized by restFC. Based on the content-appropriate specialization of the Motor network demonstrated above (Fig 5), we considered regions within this network as to-be-predicted "targets" for the emergence of neural representations driving overt behavior.

FC to these regions from the rest of the brain was estimated via MVAR in a separate resting-state EEG session. This MVAR approach was constrained via principles adapted from the causal inference [49] and causal connectivity literatures (50,51; see Methods for details) to output dynamic, lagged, direct, and directional estimates of restFC (see Fig 3A). The restFC regression weights for each participant were appropriately regularized via optimized principal component analysis (PCA) regression (results of this cross-validated optimization: cross-subject mean squared error (MSE) in predicting future resting-state activation time series = 0.006 (std = 0.003); optimal nPCs = 540 (59.4% of participants) or 1,080 (40.6%)). These lagged restFC weights were then combined with lagged task activations to generate future model-predicted activation time series for all Motor network regions across the entirety of the task (Fig 3B). The Supporting information (S1 Text) depicts the correlation-based group restFC matrix and presents some descriptive analyses verifying recovery of the canonical functional network architecture (as a sanity check), as well as the inter-subject reliability of the MVAR FC weights (Fig E in S1 Text).

We first assessed the accuracy of the dynamic activity flow model in capturing the emergence of behavioral response information in this simple categorization task. The predicted Motor region activation time series underwent the same dynamic MVPA procedure applied previously to the actual data. This yielded a predicted Motor network response information time course, which is depicted in Fig 6A along with the actual Motor time course. The plot demonstrates that overt behavioral information was decodable at multiple time points from

the predicted data which, to reiterate, was generated exclusively from FC weights derived from a held-out rest session, and held-out (past) temporal task information. The predicted decoding peak was in fact significantly higher in magnitude (82.3%) than the actual peak (79.8%), as formalized by a paired Wilcoxon contrast of the subject-level peaks (extracted from the actual group time-to-peak at 0.125 s): $z = 2.36$, $p = 0.018$. We advocate caution in inferring too much from this greater decodability in the predicted data (which, as a 2.5% peak difference, is numerically small), and in subsequent sections (accompanying Fig 6B and 6C) detail more intuitive findings of greater significance in the actual compared to the predicted data. These findings suggest that this singular instance of greater decodability in the predicted data likely arose from a trivial source, such as partial overfitting to noise.

Critically, comparison of the overlap between the predicted and actual decoding time courses confirmed that the model faithfully captured the temporal morphology of the information time course. This held at the group-level ($r = 0.97$, $p < 0.00001$) and also at the subject level ($r = 0.78$, $p < 0.00001$), further emphasizing the accurate individualized predictions obtained. The subject-level coefficient of determination (R^2, capturing scaled prediction accuracy; see Methods) was also reliably greater than 0 (mean $R^2 = 0.42$, $p < 0.00001$), indicating that dynamic activity flow modeling outperformed a null model built from the mean. Similarly high model prediction accuracy was achieved when using more common noncausal filtering during preprocessing (Fig F in S1 Text). In the Supporting information, we also highlight the utility of our rigorous regression approach to controlling for field spread artifacts, which was applied in all modeling analyses reported here to effectively control for potential leakage/circularity (see also Fig G in S1 Text).

Finally, we also compared the accuracy of our model's predictions to a permuted null model in which predicted response information time courses were generated (over 500 permutations) after scrambling the MVAR FC terms. Critically, the order of the autoregressive activation terms were preserved, to provide a targeted test of the informativeness of the FC terms specifically in accurately simulating response information. Comparing the proportion of permuted prediction accuracies greater than that observed in the unscrambled data confirmed that the FC terms were highly informative (observed $r >$ permuted r, $p = 0.002$, at group and subject levels).

The predicted dynamic MVPA results hence attest to the fidelity of the dynamic activity flow model in capturing the network-weighted flow of response information in a highly temporally resolved and individualized fashion. This highlights the utility of the modeling approach in evidencing the cognitive relevance of restFC in generating response information dynamics underlying behavior.

Dynamic activity flow modeling also predicts the raw activation time series (motor ERP)

We then probed the model's accuracy in predicting activations in Motor network regions that were the basis of the dynamic MVPA analysis. This would demonstrate fidelity to the underlying neural activation time series and challenge the possibility that the strong response information decoding in the predicted data emerged from factors artificially introduced by the model.

We targeted accurate prediction of an established motor ERP termed the lateralized readiness potential or bereitschaftspotential [52–54]: greater activation at the time of response commission for Motor network regions that are contralateral to the response hand. The predicted and actual group motor ERP waveforms are provided in Fig 6B (as contralateral minus ipsilateral difference waves; see Methods). Multiple significant activation time points were observed in the actual and predicted time courses, albeit these were anticipatedly greater in number for

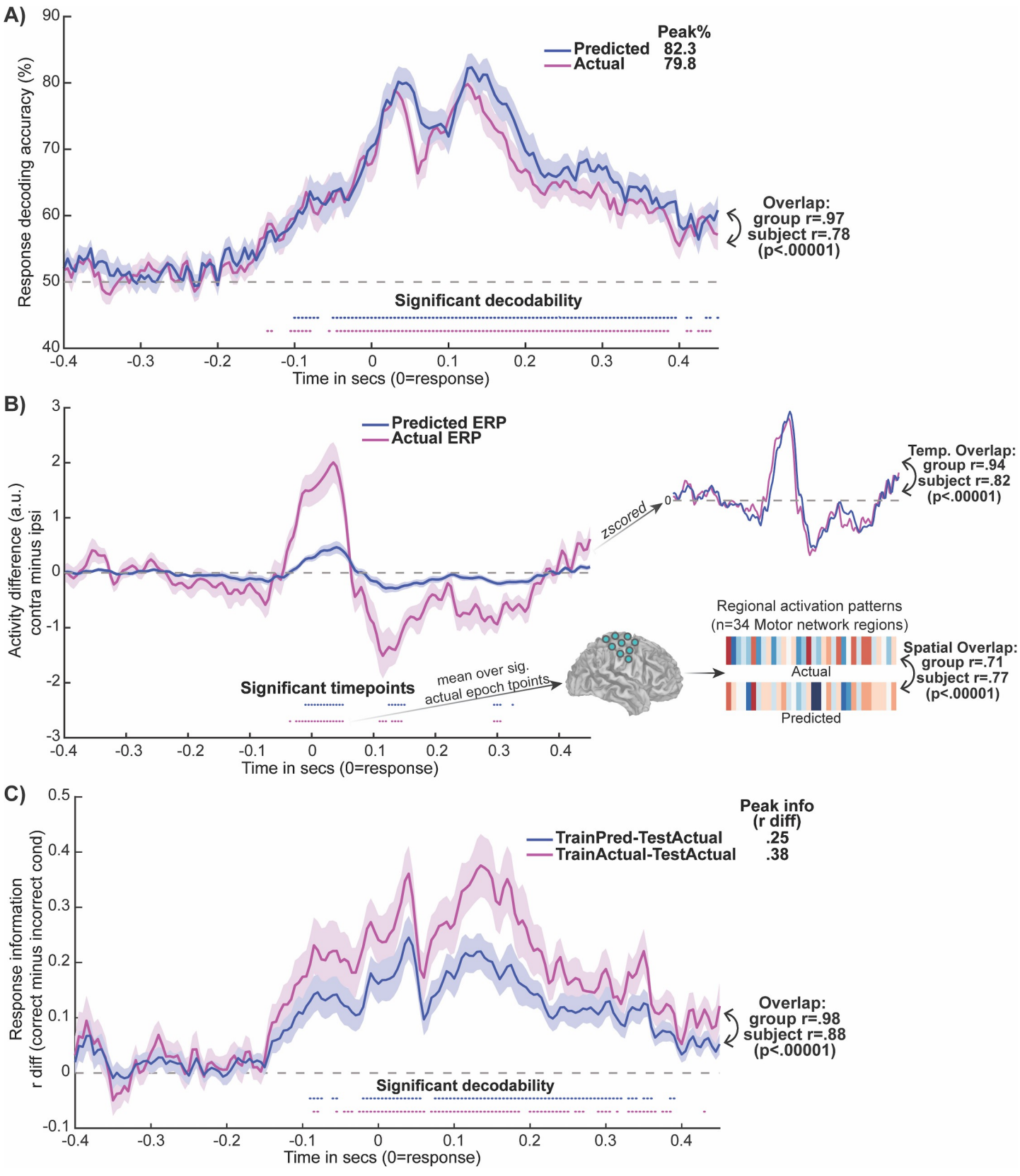
A)
Response decoding accuracy (%)
Peak%
Predicted 82.3
Actual 79.8
Overlap:
group r=.97
subject r=.78
(p<.00001)
Significant decodability
Time in secs (0=response)
B)
Activity difference (a.u.)
contra minus ipsi
Predicted ERP
Actual ERP
zscored
Temp. Overlap:
group r=.94
subject r=.82
(p<.00001)
Regional activation patterns
(n=34 Motor network regions)
Spatial Overlap:
group r=.71
subject r=.77
(p<.00001)
Actual
Predicted
Significant timepoints
mean over sig.
actual epoch tpoints
Time in secs (0=response)
C)
Response information
r diff (correct minus incorrect cond)
Peak info
(r diff)
TrainPred-TestActual .25
TrainActual-TestActual .38
Overlap:
group r=.98
subject r=.88
(p<.00001)
Significant decodability
Time in secs (0=response)

Fig 6. Dynamic activity flow modeling accurately and veridically predicts future behavioral response information. (A) The model accurately predicted future response information dynamics in the Motor network. Predicted and actual group decoding time courses are plotted, with overall decoding peaks (top right), and predicted-to-actual time course overlap (Pearson r) at group and subject levels. **(B)** The motor ERP waveform (and spatial pattern) was also successfully predicted, demonstrating fidelity to the underlying activations. Group averaged ERP difference waves are plotted (contralateral minus ipsilateral; a.u. = arbitrary units). To aid visualization, the top right depicts the z-scored group waveforms, along with the temporal predicted-to-actual overlap (at group and subject levels). The bottom right provides the spatial overlap between the predicted and actual Motor region activation vectors, extracted over the −0.035 to 0.050 s epoch of significance in the actual data. **(C)** Representational overlap analyses highlight veridicality of the model-predicted representations, given their ability to decode the actual data. The group information time course resulting from training on predicted representations and testing on the actual data (TrainPred-TestActual) is depicted, as well as the result of training and testing on the actual data (TrainActual-TestActual) for comparison. Response information was quantified as the difference in Pearson r values computed for the test activation pattern at each time point with correct minus incorrect response condition templates (see Methods). Overall information peaks (top right) and temporal overlap between the 2 time courses (bottom right) are provided. For all panels, significance at each time point was assessed via Wilcoxon sign rank tests (versus 50% chance for panel A, and versus 0 for B/C) with Bonferroni correction. Subject-level data underlying this figure are accessible via the public data repository (https://osf.io/mw4k3, subdirectory: Results_figures_data/Figure6). ERP, event-related potential.

https://doi.org/10.1371/journal.pbio.3001686.g006

the actual data. Critically, high overlap in the temporal morphologies of the predicted and actual time courses was observed at both the group and subject levels (r = 0.94 and r = 0.82, respectively, both $p < 0.00001$). We also probed the predicted-to-actual overlap in the spatial domain, by correlating the respective activation vectors for Motor network regions averaged across the epoch of significance in the actual data (−0.035 to 0.050 s, Fig 6B). This revealed a high degree of spatial overlap between the predicted and actual spatial activation patterns, at the group (r = 0.71) and subject levels (r = 0.77, both $p < 0.00001$). This high spatial overlap held when the predicted and actual vectors concatenated time points across the entire trial, at both the group (r = 0.70) and subject levels (r = 0.61, both $p < 0.00001$). Subject-level R^2 values were also reliably greater than 0, indicating superior model performance than the mean, across temporal (mean $R^2 = 0.25$, $p < 0.00001$) and spatial (mean $R^2 = 0.16$, $p < 0.0001$) overlap domains. Overall, the motor ERP results illustrate that the dynamic activity flow model maintained high fidelity to the actual task activations, across both temporal and spatial domains, and even at the individual subject level.

The model is directly faithful to the veridical representational geometry

While the previous section reported highly accurate predictions of the underlying Motor network activations, we sought to more directly demonstrate that the strong response information decoding obtained via dynamic activity flow modeling was driven by multivariate representations that overlapped with how the brain veridically represents response information. This aligns with mounting emphasis on the need to optimize representational overlap between neural network models and the brain [39,55,56].

To address this, we investigated whether actual response information in the Motor network could be dynamically decoded from the model-predicted representations. The group information time courses are presented in Fig 6C: (1) for trained representations in the predicted data applied to decode the actual data ("TrainPred-TestActual"); and (2) for trained representations in the actual data applied to decode the actual data ("TrainActual-TestActual"). The figure highlights multiple significantly decodable time points in the key TrainPred-TestActual time course, providing direct evidence that the dynamic activity flow model captured neurally valid multivariate representations. In keeping with the preceding ERP analyses, the number of significantly decodable time points (and the overall information peak) was anticipatedly higher in the TrainActual than the TrainPred model. Critically, the morphology of the resultant response information time course also temporally overlapped with that obtained for the TrainActual-TestActual model, at the group and subject level (r = 0.98 and r = 0.88, respectively, both $p < 0.00001$). Subject-level R^2 was also reliably greater than 0 (mean $R^2 = 0.59$, $p < 0.00001$). This suggests that the dynamics in representational geometry over the entire trial were well captured. Overall, this representational overlap analysis provides compelling

evidence that the dynamic activity flow model preserves high fidelity to the veridical neural codes underlying response information.

Model-simulated network lesioning suggests prominent influence of the CCNs in driving response information flow

We modified dynamic activity flow modeling to provide additional insight into the network computations that generate behavior. Separate models predicting response information in the Motor network were run that systematically lesioned all but one of the remaining functional networks, while also excluding the autoregressive/self-coupling terms (see Methods). Beyond this iterative restriction of source predictor terms (Fig 3B), the procedure was identical to that detailed in the dynamic MVPA analysis of the model-predicted data. This yielded 10 response decoding time courses for each functional network model, capturing their putative influence on information flow to the Motor network. We then adopted a model comparison approach (similar to earlier network modeling approaches e.g., [57]) to identify which networks were the most prominent drivers of response information flow to the Motor network in this simple task, via rigorous statistical comparison of the information peaks across networks with multiple comparison correction.

The network-lesioned group decoding time courses are presented in Fig 7A. Visual inspection revealed significant decodability for all network models; however, this peaked highest for the CCN models (top right Fig 7A), with onset also preceding the other networks (top left Fig 7A). The time courses once again followed a 2-peak morphology, with CCN-derived decodability visibly varying across the earlier motor preparation epoch and the later motor execution/feedback epoch (as in Fig 5).

However, these network lesioning analyses critically extended the descriptive results in Fig 5, highlighting that while the CCNs exerted a broadly strong predictive influence across the trial, this pattern of influence differed across the 2 peaks. These differing network profiles were statistically formalized by between-network contrasts (model comparisons) of subject-level predicted decoding peaks, which were extracted separately from identifiable group peak time points for peak 1 (0.045 s) and peak 2 (0.155 s). At the motor preparation peak 1 (Fig 7B), the DAN network model yielded response decodability that was significantly higher than the CON ($p < 0.05$ false discovery rate [FDR] corrected, Fig 7C) and marginally higher than the FPN ($p < 0.05$ uncorrected). Considering the strong influence of the Visual network also observed at peak 1 (Fig 7B), the results again support more selective engagement of the DAN during this likely period of sensory-related processing (e.g., translating sensory into response information). At the later motor execution/feedback peak (Fig 7D), all 3 CCNs exerted the strongest generative influence on response decodability and were not reliably differentiated among each other (Fig 7E), even at lenient $p < 0.05$ uncorrected thresholds. The pattern of network model differences again suggests more collaborative engagement across the CCNs, possibly reflecting the formation of purer response representations during this later period.

The network lesioning results therefore extended previous description of spatiotemporal signatures underlying response information to elucidate the generative influence of the CCNs on network information flow driving overt behavior. This prominent influence of the CCNs was also recovered when using subject-level prediction accuracy for each network model as an alternative metric to the predicted decoding peaks used above (Fig H in S1 Text).

Actual and model-predicted results hold with reduced numbers of EEG electrodes

We explored the effect of varying analysis parameters on the results. First, we reduced the numbers of available EEG electrodes by confining the preprocessed causal filter data to

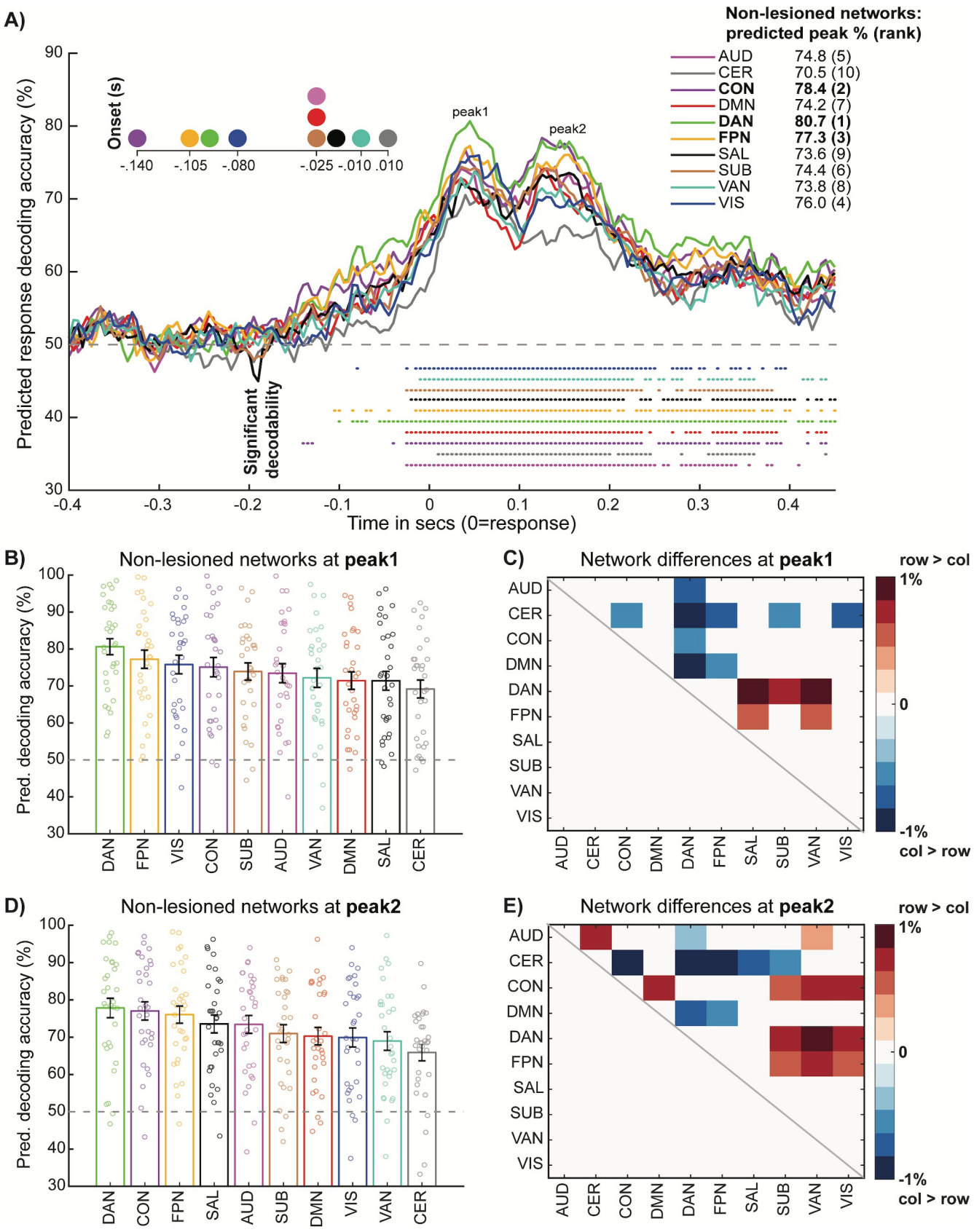
A)
Non-lesioned networks:
predicted peak % (rank)
AUD 74.8 (5)
CER 70.5 (10)
CON 78.4 (2)
DMN 74.2 (7)
DAN 80.7 (1)
FPN 77.3 (3)
SAL 73.6 (9)
SUB 74.4 (6)
VAN 73.8 (8)
VIS 76.0 (4)
Onset (s)
-.140 -.105 -.080 -.025 -.010 .010
peak1
peak2
Significant decodability
Predicted response decoding accuracy (%)
Time in secs (0=response)
B)
Non-lesioned networks at peak1
Pred. decoding accuracy (%)
DAN FPN VIS CON SUB AUD VAN DMN SAL CER
C)
Network differences at peak1
row > col
col > row
D)
Non-lesioned networks at peak2
DAN CON FPN SAL AUD SUB DMN VIS VAN CER
E)
Network differences at peak2

Fig 7. Network lesioning reveals contributions of individual functional networks in driving future behavior. Unlike the visually similar Fig 5 that provided descriptive insight, these analyses provided explanatory insight into which spatial networks likely drive response information representations in the Motor network and their accompanying temporal signatures. For these analyses, all networks were lesioned except for the indicated (non-lesioned) network. **(A)** Group predicted decoding time courses for each of the network-lesioned models, color-coded by affiliation as before. Magnified decoding onsets (top left), overall decoding peaks (top right) and significant decodability at each time point (assessed via Bonferroni corrected Wilcoxon tests, as before) are provided for each network model. **(B)** Predicted response decoding accuracy ranked across network models at peak 1 (0.045 s). Each bar represents the mean and standard error for each network, with overlaid subject data points. **(C)** Matrix capturing cross-network differences in predicted decoding accuracy at peak 1. Plotted is the pairwise difference in mean decoding accuracy, thresholded via paired Wilcoxon ($p < 0.05$, FDR corrected). Positive values denote significantly higher predicted decoding accuracy for the row network > the column network, and vice versa for the negative values. **(D)** and **(E)** follow the same conventions as (C) and (D), respectively, except now focusing on peak 2 (0.155 s). Subject-level data underlying this figure are accessible via the public data repository (https://osf.io/mw4k3, subdirectory: Results_figures_data/Figure7). FDR, false discovery rate.

https://doi.org/10.1371/journal.pbio.3001686.g007

standard 64- and 128-electrode montages, to test the generalizability of our source modeling and dynamic activity flow network modeling approaches across available EEG systems. To derive these montages, the spatial euclidean distance between template coordinates for each electrode in the 64-/128-electrode systems and electrode coordinates in the original 256-electrode system was computed. The 256 system electrode with the minimum euclidean distance with a given electrode in the 64/128 system was uniquely assigned to it.

For the SourceAll versus SensorAll response decoding analysis, we recovered the original finding of higher peak information decodability for source data across both reduced electrode montages (see Fig 8A, which includes the results for the 256 system for reference). However, the group information peak in the source data increased with increasing numbers of electrodes (see panel in Fig 8A). This conclusion was quantified by extracting unbiased information time course peaks at the subject level (as before) and submitting them to a 3 (electrodes: 64, 128, and 256) × 2 (data type: sensor and source) repeated measures ANOVA. This revealed a main effect of data type that confirmed the superiority of source compared to sensor information decoding across electrode numbers (subject source peak mean = 89.0%, sensor peak mean = 84.9%, $F(1,31) = 29.29$, $p < 0.001$, $n^2_G = 0.079$). The main effect of electrodes was nonsignificant ($F(2,62) < 1$). We also observed a nonsignificant interaction, suggesting a trend toward increasing source versus sensor superiority with increasing number of electrodes ($F(2,62) = 2.90$, $p = 0.063$, $n^2_G = 0.003$). Planned paired Wilcoxon contrasts of source peaks across the 3 electrode types were nonsignificant, but suggested a numerical "jump" in source decodability for 128 and 256 systems compared to the 64 system (source 128 versus source 64, $z = 1.65$, $p = 0.102$; source 256 versus source 64, $z = 1.70$, $p = 0.092$; source 256 versus source 128, $z = 0.80$, $p = 427$). Hence, the central finding of greater source compared to sensor decodability held with reduced numbers of electrodes. This complements the more fundamental benefit of source modeling in allowing for more valid spatial inferences (a prerequisite for our network decoding and dynamic activity flow modeling analyses), whereas sensor-level analyses are inherently spatially ambiguous. We also found a numerical (albeit in this case statistically unreliable) increase in the magnitude of this source advantage for systems with greater than 64 electrodes.

We also repeated the main dynamic activity flow modeling analysis for the reduced 64- and 128-electrode systems. Fig 8B plots actual and model-predicted Motor network response information time courses across the 3 electrode systems. Again, we find that the main modeling results hold even when fewer electrodes are available: dynamic activity flow modeling reliably predicted response information (multiple significantly decoded time points in the predicted time courses) and accurately captured the temporal morphology (significant subject-level predicted-to-actual overlap r values; see panel of Fig 8B). However, actual and predicted group peak decodability numerically increased with greater numbers of electrodes (see panel of Fig 8B), as did the number of significantly decodable time points. We quantified these impressions

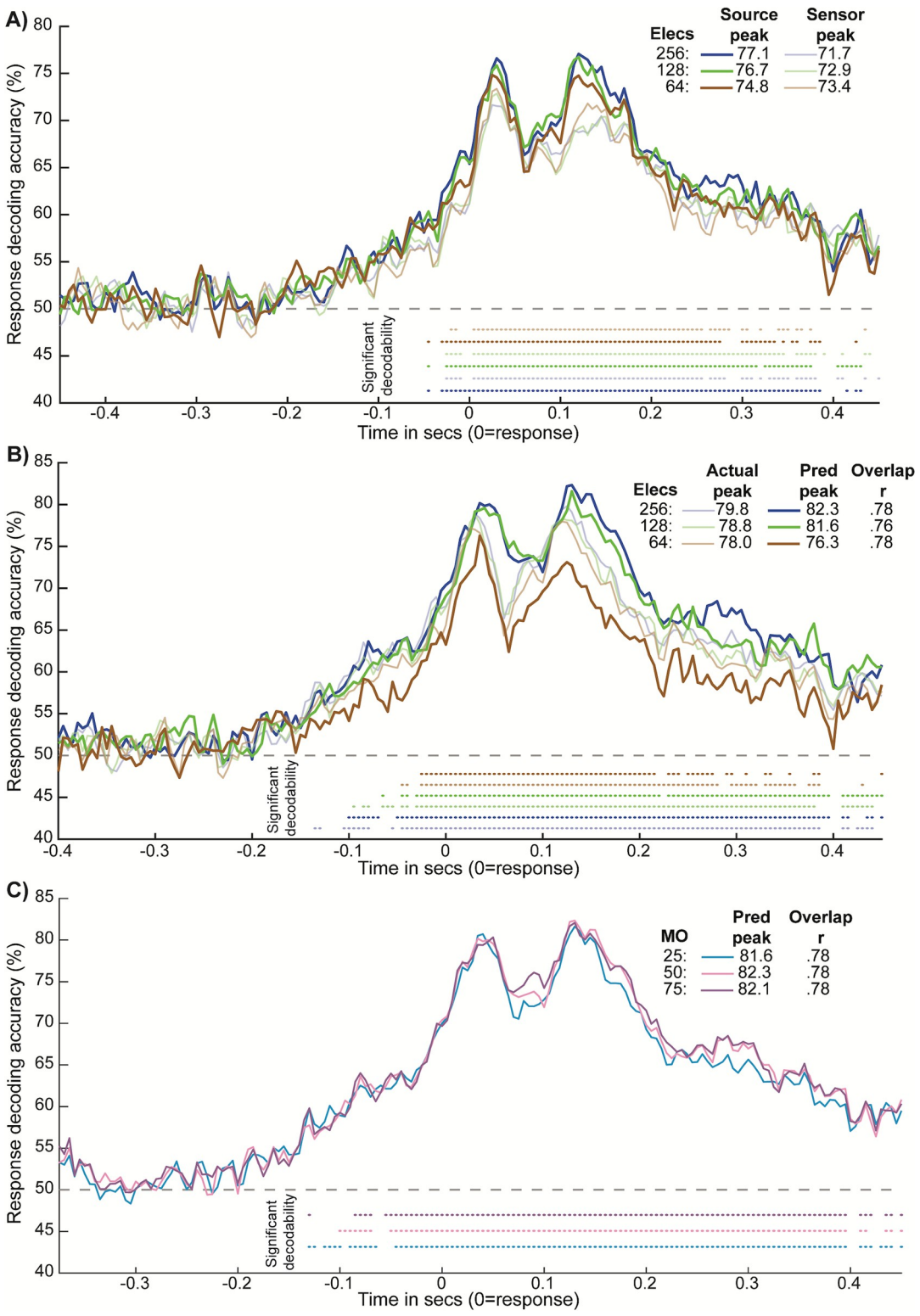

Fig 8. Control analyses varying number of electrodes and model order. (A) Group response decoding time courses for the SourceAll (dark lines) and SensorAll (softer lines) feature sets, plotted across variation in number of available electrodes (color-coded). **(B)** Group response decoding time courses for actual (softer lines) and model-predicted (darker lines) Motor network information, plotted across electrode systems. Note that subject-level predicted-to-actual overlap r values are also provided in the legend (all $p < 0.00001$). **(C)** Group response decoding time courses for model-predicted Motor network information

across variation in model order (MO; number of lagged predictors). Subject-level predicted-to-actual overlap r values are also provided in the legend (all $p < 0.00001$). For all panels, significantly decodable time points and group peak decoding accuracies are depicted per conventions in the earlier figures.

https://doi.org/10.1371/journal.pbio.3001686.g008

via paired Wilcoxon contrasts of unbiased subject-level information time course peaks across electrode systems. Whereas none of the pairwise contrasts of the actual Motor network peaks were significant ($p < 0.600$ for all), contrasts of the predicted data revealed significantly greater information peaks for the 256 versus 64 systems (4.0% peak change, z = 3.78, $p < 0.001$) and for the 128 versus 64 systems (3.5% peak change, z = 4.33, $p < 0.001$), but not for the 256 versus 128 systems (0.5% peak change, z = 0.58, $p = 0.570$). Contrasts of the subject-level prediction accuracy (i.e., predicted-to-actual temporal overlap r values) were all nonsignificant ($p > 0.140$ for all). Hence, while the amount of response information detectable by dynamic activity flow modeling increased with >64 electrodes, the ability of the model to capture the accompanying temporal dynamics was equivalently accurate.

The results coalesce with the source versus sensor contrasts in Fig 8A to suggest that the key findings are reliably recovered even with fewer electrodes, highlighting the robustness of our source decoding and activity flow modeling approaches across variable EEG electrode systems. However, both analyses also suggested that the strength of recovered effects increases with greater numbers of electrodes, with a prominent "jump" when using greater than 64 electrodes and more modest differences between 128 and 256 systems. This pattern has been observed in previous source modeling reports [58,59].

Dynamic activity flow modeling is equivalently accurate across variation in model order

We also explored the effect of varying the model order parameter that determined the number of lagged predictors entered into the MVAR restFC estimation and subsequently the number of lagged activation terms used in dynamic activity flow modeling (see Fig 3). The modeling was rerun over both shorter (5 lags i.e., 25 ms) and longer (15 lags i.e., 75 ms) model orders. Note that the computationally intensive nature of MVAR restFC estimation meant that we had to reduce the available parameter space in a principled manner wherever possible to ensure tractability. Hence, we referenced prior relevant literature and our own work involving autoregressive modeling (see Methods for details) to select the 10 lags (50 ms) model order for the main analyses. Nevertheless, these control analyses revealed that the dynamic activity flow modeling predictions were equivalently accurate across variation in model order. Fig 8C plots the model-predicted response information time courses across the 3 model orders, which were visibly similar and yielded equivalent group peaks (see figure legend). Paired Wilcoxon contrasts across the 3 model orders revealed no significant differences in the amount of model-predicted information captured by each model ($p > 0.350$ for contrasts of subject-level predicted time course peaks) nor the ability of the model to capture the morphology of the response information dynamics ($p > 0.600$ for contrasts of subject-level predicted-to-actual overlap r). Hence, the accuracy of dynamic activity flow modeling held across variation in model order.

Discussion

The present report serves as a first demonstration of a dynamic activity flow network modeling approach capable of elucidating, in spatiotemporally resolved fashion, the network computations that give rise to multivariate information representations underlying behavior in the

human brain. In developing this modeling technique, we benefited from recent advances in anatomically individualized EEG source modeling [44,60], which we combined with dynamic MVPA to decompose spatially "where" and temporally "when" task information (specifically, response and sensory information) was present across the entire brain. This extended prior applications of dynamic MVPA in sensor-level EEG, which is inherently incapable of elucidating the spatial loci of neural coding schemes and is contaminated to a greater degree (relative to source EEG) by field spread artifacts [61,62]. Beyond fulfilling our need for valid spatial reconstruction, we observed generally improved information detection when sources were treated as MVPA features rather than sensors, and this held across variation in available EEG electrodes (see Fig 8). This finding should motivate increased application of source modeling in dynamic EEG/MEG decoding studies moving forward.

Our combination of source EEG and dynamic MVPA enabled us to probe the large-scale human analogues of population coding schemes reported in animal electrophysiology research. While the spatial resolution of these invasive methods remains considerably higher than our noninvasive approach, we nevertheless were able to decode with equivalent temporal resolution and superior whole-brain coverage in humans. Maximizing whole-brain coverage is non-trivial, given that regions not implanted with recording electrodes are effectively missing from descriptive maps of information content, and more critically can act as unobserved confounders (adopting the language of causal inference, 49) in modeling how task information emerges. Our network decoding approach revealed broad representation of stimulus and response information across all major functional networks, paralleling the spatially distributed information profiles reported in animal studies [9–13]. Despite this broad decodability, analysis of the information peak and temporal onset revealed a degree of network specialization: response information emerged earliest and maximally in the Motor network, and sensory information emerged earliest and maximally in sensory networks. Our findings align with recent electrophysiological research challenging a strictly compartmentalized or modular view of functional organization (which would not anticipate spatially distributed information), in favor of a more graded organization [10,13]. While we are confident that our rigorous acquisition and analysis steps mitigated the influence of field spread and associated spatiotemporal leakage of neural information, future applications of our model in nonsource EEG modalities (e.g., human electrocorticography, ECOG, data) would further strengthen these inferences. The simplified nature of the present sensory–motor categorization task is also worth emphasizing, and future applications of our methods to more complex tasks (and hence decoding of more complex forms of multivariate information, such as task rule/context) will be critical in interrogating the generalizability of our functional inferences. This includes our interpretation of the 2-peak response decoding morphology (shown to be representationally distinct in our temporal generalization analysis, panel C of Fig C in S1 Text) as reflecting early motor preparation and later motor execution/feedback processes respectively. While this inference is supported by findings from animal electrophysiology and scalp EEG [11,47,48,63,64], it remains to be seen whether similar dynamic network profiles are elicited when responses are generated in different, more complex tasks.

Our dynamic activity flow network modeling analyses marked a significant advance over merely decoding task information, through formalizing a model of how that information is computed and transferred across the brain—a lacuna in the information decoding literature highlighted previously [21,22,39]. The model accomplishes this by using connectivity estimated empirically during task-free rest to parameterize a neural network architecture, wherein these connectivity estimates weight the likelihood of task information propagating to Motor network regions from the rest of the brain. This activity flow model implemented key output innovations compared to previous versions [16,30,31]. First, the model produced fully

dynamic outputs of behavioral response information (with millisecond-scale resolution), unlike previous versions that predicted trial-averaged fMRI beta activations. Extending to fully dynamic predictions was facilitated by application in high temporal resolution source EEG data, and indeed the success of the model in this imaging modality (the first application in a non-fMRI modality) testifies to its general validity. A second output refinement was that predictions of future information dynamics were accomplished through a multivariate autoregression framework (past lagged task activations weighted by lagged restFC). Predicting the future information state of the brain represents a significant advance over more standard approaches of predicting held-out data at the same trial time point, given that this integrates a fundamental principle of causality and the direction of time (i.e., causes temporally precede effects; 49,65,66). Applying this future-predicting property to simulate the generation of response information ensured functional significance (albeit limited to this simple task context), given that this information drove participants' overt behavior [21,67].

The above output features (fully dynamic and prospective predictions) bring the activity flow framework into the realm of ANN models that have emerged as the dominant method of simulating cognitive information in artificial intelligence [55,56,68]. A critical benefit of our approach over these artificial models is its foundation in empirical data, which enabled (1) empirical estimation of network connectivity weights; and (2) direct comparison of model-derived representational geometry with actual empirical data.

Regarding the first point, our ability to simulate future information dynamics in a more causally interpretable way (via past activations propagating over lagged restFC) was critically dependent on more causally interpretable estimation of restFC [69]. We used an autoregressive form of multiple linear regression to estimate parameters capturing dynamic, lagged, direct, and directional connectivity between brain regions. This yielded more interpretable and neuroscientifically valid connectivity weights than those estimated in ANNs via random initialization and intensive optimization. The fact that these connectivity weights generalized from predicting future activations in the rest data (implicit in how FC estimates were regularized; see Fig 3A and Methods) to making similar predictions during task performance attests both to the intrinsic (state-general) functional network architecture present at rest [70,71], as well as the utility of autoregressive methods in capturing it [72–74]. Functionally, the success of dynamic activity flow modeling provides strong evidence of the cognitive relevance of restFC [32], which yielded accurate predictions even in this difficult scenario of simulating future information dynamics in high temporal resolution data. The results therefore support the hypothesized role for restFC as a large-scale analogue of synaptic weight processes that coordinate information processing across the brain [8,23,27].

A second benefit of our empirical modeling approach over ANNs is that it enabled direct assessment of the overlap of model-derived representations with those instantiated in the human brain. Given that the degree of computational flexibility is high even in dramatically simplified neural networks [75], this raises the possibility that accurate simulation of task information might arise from nonveridical representational codes [21,38,39,55]. To address this, we demonstrated reliable decoding of the actual data from the model-predicted representations. Predicting outputs in the same neural units as the empirical data (i.e., task activation representations in the Motor network) simplified the process of comparing the predicted and actual representational geometry, in comparison to the abstract units in ANNs. With continued advancement in computing hardware and access to large training datasets, it seems likely that ANNs will yield accurate simulations of increasingly complex neurocognitive phenomena. It is therefore vital that future ANNs aspiring toward neuroscientific insight are interrogated for their neural veridicality, rather than judging them solely on their ability to perform cognitive tasks.

Our final extension of dynamic activity flow modeling to simulate lesioning of different networks represents a particularly powerful approach (in our opinion), given that it allows for formal testing of multiple candidate neural network models in empirical data. This model comparison approach suggested a prominent role for the CCNs in representing behavioral response information: activity flow models built selectively from these 3 networks yielded the highest predicted response information with the earliest onsets. The high spatial and temporal precision obtained allowed us to uncover a dynamic network profile that separated the 3 CCNs, with early selective DAN engagement (possibly reflecting motor preparation) followed by collaborative cross-CCN engagement (possibly reflecting motor execution/feedback) in the generation of behavior.

While the implied roles for the CCNs are partially consistent with previous fMRI findings linking the DAN preferentially to sensory control [16,76], the CON to motor control [77] and the FPN to flexible task control more generally [78,79], separating these networks based on the precise timing and geometry of response representations was uniquely accomplished by our method's superior temporal resolution. This separation of the CCNs by their dynamic representational profiles suggests a degree of specialization among these networks within their broader cognitive control functionality, which will require future applications of dynamic activity flow modeling in more complex tasks to elucidate. Future extensions of our modeling approach might also target the role of the CCNs in the emergence of information in the more formal sense, by disambiguating when/how new information emerges in the brain, versus charting the spread of information after its initial emergence. This will likely require refinement of dynamic activity flow modeling to integrate nonlinear operators [12,68]. Recent source modeling validations using intracranial recordings as ground truth neural generators have demonstrated reasonably accurate (approximately 14 to 24 mm) EEG reconstruction of subcortical regions [46,80], opening up future extensions of our modeling approach at this deeper and more fine-grained spatial scale, beyond the cautious network-level focus adopted for this first demonstration. A greater emphasis on subcortical regions would also benefit from more recent functional atlases that achieve more exhaustive subcortical parcellations [81,82] and task paradigms that are established in engaging subcortex (e.g., medial temporal lobe activity during long-term memory tasks).

To reiterate, our modeling framework imposed certain constraints on its computations (via more causally interpretable estimation of restFC) and outputs (fully dynamic and prospective predictions of behaviorally relevant response information). This was furthered in the lesioning analysis through simulating perturbations to the system, as an analogue to classical lesioning approaches in neuropsychology [83] and disruptions to neural processing induced by brain stimulation techniques (e.g., transcranial magnetic stimulation [TMS] and transcranial alternating current stimulation [TACS]). Note that the latter class of methods will undoubtedly be necessary to verify the accuracy of our simulated lesioning results, which at present merely serve to propose candidate network computations underlying response information flow. For example, stimulation methods can enact causal perturbations of the brain to clarify whether inhibiting (via TMS [84]) or desynchronizing (via TACS [85]) CCN regions during task performance disproportionately disrupts the emergence of response information and behavior, relative to disrupting other networks.

This potential for dynamic activity flow modeling to generate predictions for stimulation interventions raises more general utility in empirically deriving individualized network models of a particular cognitive function. The efficacy in individualizing the models is demonstrated by our consistently high subject-level prediction accuracy and previous reports highlighting the highly individualized "trait" information contained in restFC [86,87]. The simulated lesioning approach gives a particularly clear example of how individualized network models

can be manipulated/perturbed to generate insights into individuals' neural coding profiles. Beyond providing theoretical insight into computational principles of task information, such modeling could be useful in modeling dysfunction in clinical contexts, and the successful implementation of the network models in empirical human imaging data makes this clinical translation easier than for abstract ANNs [31,88]. In achieving this long-term clinical aim, we reiterate that future work will undoubtedly be necessary to test the efficacy of dynamic activity flow modeling in simulating information in more complex and naturalistic tasks, and in clinical disorders. Nevertheless, our preliminary findings attest to the potential of harnessing the causal inference tenets of this framework to build accurate, individualized models of neurocognitive function in health and disease.

Methods

Participants and study design

The sample consisted of 32 healthy young adults (age mean = 21.50 years, range = 18 to 30; 14 female) out of a total of 33 recruited (one participant was excluded due to a computer malfunction aborting their session). All participants provided informed written consent prior to participating, as per the ethical guidelines from the Rutgers University Institutional Review Board (IRB).

Each participant took part in 2 sessions: an MRI session (in which T1 structural MRI images were collected for EEG source modeling, in addition to T2 structural and 10-minute resting-state fMRI sequences) and an EEG session (consisting of 10-minute pre-task resting state, approximately 35 minute task and 10-minute post-task resting-state sequences). The fMRI resting-state and EEG post-task resting-state sequences were not analyzed for the present report.

MRI and EEG data acquisition

MRI data were acquired using a 3T Siemens Trio scanner housed at the Rutgers University Brain Imaging Center (RUBIC), with a 32-channel head coil. From the full MRI session (see Participants and study design section for details), only the T1 structural images (MPRAGE, 0.8mm isotropic voxels) were used in the present report to construct realistic head models for EEG source modeling.

EEG data were acquired using the HydroCel Geodesic Sensor Net (HC-GSN) dense-array system manufactured by EGI (1000 Hz sampling rate, 256 sensors, Cz reference electrode). Saline solution was used as electrolyte, and impedances across all channels were lowered to <50 kΩ at the start of the session. All resting-state and task components of the experiment were presented to participants on a laptop running Eprime 2. To minimize fatigue and related artifacts (e.g., electromyographic, EMG, artifacts), participants were seated in a comfortable chair and were allowed to rest freely between task blocks.

Task design

For the EEG pre-task resting-state session (used to estimate FC weights for the dynamic activity flow model; see later Methods sections), participants were instructed to rest while fixating centrally and to not fall asleep. The ensuing EEG task session consisted of a cued sensory categorization paradigm with a 2-alternative forced choice response format (2AFC; see Fig 1 for design schematic). Participants were cued at the start of each block as to which sensory modality would be presented on the ensuing block of 10 trials and the associated stimulus-response mappings: visual (horizontal versus vertical lines) or auditory (low versus high pitch tones).

Participants responded with the left or right index fingers across both sensory modalities, with stimulus-response mappings held constant (e.g., horizontal lines were always categorized with the left index finger). The interval between the cue and first block was randomly jittered (5.5, 6, or 6.5 s in duration). On each trial, participants had 1 s to respond after stimulus onset, followed by a randomly jittered inter-trial-interval (1, 1.5, or 2 s). The order of visual and auditory sensory conditions was randomized across blocks.

Causal temporal filtering prevents circularity in dynamic activity flow modeling

Importantly, all temporal filters applied in the EEG preprocessing pipeline used a "causal" filter design [89–92]. This prevented circularity from entering into our dynamic activity flow modeling analysis (see later Methods section) due to leakage of task information from the present time point (t0) to past lagged time points (t0-n lags) after filtering. Such leakage could arise from more commonly applied "noncausal" filters, wherein through both forward and backward application of the filter its output at t0 is influenced by both past (t0-n lags) and future (t0+n lags) time points. The backward step involving future time points could introduce circularity into our autoregressive dynamic activity flow modeling approach, from to-be-predicted target region activity at time point t0 leaking into t0-n lagged time points. This could lead to the target t0 time points being predicted to some degree by themselves. To eliminate this possibility, we used a causal filter design (1-pass, hamming-windowed, minimum phase finite impulse response (FIR; [91]), which only used past time points to calculate the output time points at t0. This allowed us to benefit from the critical improvements in artifact removal and signal-to-noise ratio resulting from temporal filtering, while not introducing circularity into the modeling analyses.

A limitation of causal filtering is the introduction of a delay in the filtered output signal relative to the input [91,93]. Hence, we advocate caution in inferring too much into the precise absolute timing of the reported activation and information time courses; rather, we focus on comparisons of relative timing (e.g., comparing information decoding onset across spatially distinct functional networks, which have all undergone identical causal filtering and hence are subject to equivalent output delays). Nevertheless for completeness, in the Supporting information (Fig F in S1 Text) we provide a full set of results after application of more conventional noncausal filters during preprocessing (design: 2-pass, hamming-windowed, zero-phase Butterworth (infinite impulse response, IIR)). Given that noncausal filters are designed to correct for output latency delays by backward application of the filter, and as these filters are more commonly applied in EEG/MEG research, these supplemental results should provide some means of comparing the absolute timing of our decoding results with previous reports. Albeit it is again worth highlighting the supplementary nature of these results, given their potential for introducing leakage/circularity in the dynamic activity flow modeling results. We also encourage caution in inferring too much into absolute timing even for the noncausal filter results, as previous studies have established that these filters in practice overcorrect for the latency delay by shifting the onset of signals prior to when they actually occur [89].

EEG preprocessing

All EEG preprocessing was conducted in Matlab using the Fieldtrip toolbox [94], with an identical pipeline run on the pre-task rest and task data (see Fig 2 for an overview). Notch filtering was firstly applied to the continuous data to remove line noise (cutoffs at 60 Hz and higher harmonics 120 Hz and 180 Hz), followed by high-pass filtering (1 Hz cutoff). For all filters, a causal filter design was used (as detailed in the preceding section), and filter order was

optimized in a lower-level Fieldtrip function to ensure the highest slope for the cutoff frequencies. Noisy sensors were then identified via an automated procedure, wherein all sensors with a z-scored mean absolute amplitude (across all time points) greater than 3 were removed. The continuous data were segmented into trials: −0.5 to 1.5 s for the task data around trial stimulus onset and into 20s nonoverlapping "pseudo-trials" for the rest data. Noisy trials/pseudo-trials were identified via a similar automated procedure: all trials with a z-scored mean absolute amplitude (averaged across all trial time points and sensors) greater than 3 were removed.

Temporal independent component analysis (ICA) [95] was used to identify eye blink and eye movement artifacts. Extended ICA was run on each participant's task and rest data using the "binica" method, accessible in Fieldtrip via an EEGLAB plugin [96]. After estimating the component scores, a semi-automated procedure was used to identify components capturing ocular artifacts. Two vertical electrooculogram (EOG) channels located above and below the right eye were subtracted from each other to provide a time course capturing blink artifacts with a high signal-to-noise ratio [97]. Similarly, 2 horizontal EOG channels located adjacent to the right and left eyes were subtracted from each other for the eye movement/saccade time course. These vertical and horizontal EOG signals were used as "artifact templates" that were separately correlated with each ICA component score's time course (following a similar approach in [98]), with likely artifact-related components identified as those with a z-scored absolute Pearson r value > 3. These candidate artifact components were finally accepted/rejected after visual inspection. The ICA-cleaned data were then low-pass filtered (50 Hz cutoff) to reduce high frequency artifacts (e.g., EMG artifacts which peak in the 50 to 100 Hz range; [99]), baseline corrected (treating −0.5 to 0 as the baseline for the task trial data, and the mean over each entire pseudo-trial as the rest baseline) and re-referenced to the common sensor average.

EEG source modeling

The preprocessed task and rest EEG data then underwent source modeling to recover the underlying neural source activations from the sensor signals (Fig 2). Source modeling was critical for analyses requiring valid recovery of spatial signatures of task information representation versus relying on sensor-level analyses that are inherently spatially ambiguous [61,62,69,100]. This endeavor was helped by our use of a dense-array EEG system (256 sensors), given that such a high number of sensors has been previously shown to improve EEG source localization accuracy to match the millimeter precision observed with MEG [44–46,74,101].

Realistic, individualized head model construction began by segmenting the anatomical T1 MRI images for each participant into 5 skull tissue types (gray matter, white matter, cerebrospinal fluid, skull, and scalp). This enabled finite element modeling (FEM; 60) of the distortion of electric dipole fields generated by neural activity as they propagate through skull tissues toward the scalp sensors. The FEM head model was then aligned to the dense array EEG sensors based on common fiducial landmarks. Source region locations were specified in MNI space based on the whole-brain functional atlas described by Power and colleagues [43], which provides independent functional network affiliations for 264 regions. These network affiliations were identified via clustering analyses applied to task and resting-state fMRI data in the original paper and have subsequently been verified via alternative [102] and multimodal [81,103] human parcellation approaches. Convergent network profiles have also been observed in animals [104,105], highlighting the general validity of this functional atlas. The source regions were aligned linearly with the head model and sensors. The full forward model was then estimated via normalized leadfields describing electric field propagation from the neural sources through skull tissues to the recorded EEG electrodes.

Beamforming in the time domain via the linearly constrained minimum variance approach (LCMV; [42]) was used to invert the forward model and reconstruct the activation time series for each source location. We opted for beamformer-based source modeling as this has been shown to mitigate artifactual field spread influences in source connectivity analyses, compared to alternative minimum norm estimate (MNE) approaches [33]. The orientation of the reconstructed source time series was constrained to the direction yielding maximum power (based on singular value decomposition of the 3-dimensional xyz dipole moments). This entire source modeling procedure was applied separately to the task and rest EEG data, reconstructing the relevant activation time series for each session from the same 264 spatial locations.

Dynamic MVPA

The source-modeled task EEG data were then submitted to dynamic MVPA to decode task information with millisecond-scale temporal resolution. The analyses focused primarily on decoding behavioral response information (left- versus right-handed responding, Fig 1) from response-locked data, but decoding of sensory information (visual versus auditory stimulation) from stimulus-locked data were also conducted as a supplementary analysis (see Fig A in S1 Text). The features used for dynamic MVPA were separately "SensorAll" (time series from all 256 EEG channels), "SourceAll" (time series from all 264 source regions localized from the Power atlas) or "network sources". For the latter, dynamic MVPA was performed for each of the 11 Power atlas networks separately (treating within-network source regions as features), yielding 11 information decoding time courses. Note that for all analyses targeting inferences at the network level (i.e., the network decoding and all dynamic activity flow modeling analyses), we excluded all regions from the "Uncertain" and "Retrieval" Power atlas networks, given that these networks have not been reliably recovered in more recent parcellation schemes (e.g., 81). For similar reasons, we collapsed the original "Somatomotor-hand" and "Somatomotor-face" (depicted in orange in Fig 2, panel iii) networks into a single "Motor" network definition.

The steps adopted were the same across these feature sets. For response information decoding, the trial data were first rearranged from stimulus- to response-locked (segmented −0.45 to −0.45 seconds around response commission), using the trial reaction times. The data were then downsampled from 1,000 Hz to 200 Hz (by taking every fifth sample sequentially) to boost signal-to-noise for the classifications (as recommended in 4). Incorrect trials were removed and the remaining trials arranged into the 2 conditions of interest: correct left and correct right response trials, collapsed across visual and auditory stimulation conditions. For each response condition, trials were averaged into smaller "subtrial" sets to boost signal-to-noise for the classifications [4]. Specifically, the approximately 120 trials in each condition were averaged over nonoverlapping sets of 14 trials to yield approximately 8 independent subtrials per condition, per participant ("~" reflects variable removal of noisy and incorrect trials across participants during preprocessing). The trial indices going into these subtrial averages were randomized over 10 iterations (while preserving nonoverlap within each iteration), meaning that the entire decoding analysis was run 10 times per participant to ensure robustness of the resulting information time course.

Within each of the 10 subtrial averaging iterations, linear support vector machine (SVM) classifiers were trained separately at each trial time point to distinguish between left- and right-handed responses, as implemented by libSVM [106] and the cosmoMVPA toolbox [107]. Moreover, 10-fold cross-validation was used, in which trials were pseudorandomly split into 80% training and 20% testing sets in each of 10 folds, with the constraint that no unique combination of train and test trial indices were repeated across folds. Note that the number of training trials were rounded up (e.g., 20% of 8 available trials = 1.6 = 2 training trials per

condition) and the number of testing trials were rounded down (e.g., 80% of 8 trials = 6.4 = 6 testing trials per condition), following the default behavior of cosmoMVPA. Note also that the number of train/test trials selected from each response condition was equated on each fold to prevent imbalanced trial counts from influencing the classifiers [108]. The accuracy (%) in classifying between left- and right-handed responses was averaged over folds, with this classification process repeated for each individual time point to yield a decoding time course capturing response information dynamics for that participant. The final decoding time course for each participant was taken as the average across the 10 subtrial averaging iterations. To summarize, the subtrial averaging procedure was looped 10 times (with randomized initial trial indices), with 10-fold cross-validation then initiated separately within each subtrial loop, and the decoding results averaged across the cross-validation folds and subtrial loops to derive the information time course for that participant.

Statistical significance was assessed via a nonparametric approach treating participants as a random effect, wherein the classification accuracies at each time point were contrasted against chance classification (50%) via the Wilcoxon sign rank test [4]. The resulting *p*-values were Bonferroni corrected for multiple comparisons across time points. For analyses contrasting decoding peaks via paired Wilcoxon sign rank tests, peak classification accuracies were extracted from each participant's decoding time course from the relevant group time-to-peak (see Results for details).

The Supporting information provides a number of other network decoding analyses, primarily conducted to validate the spatial accuracy of source modeling: decoding of sensory information (visual versus auditory stimulation) from stimulus-locked data (Fig A in S1 Text, panels B–D); decoding of stimulus information (visual: horizontal versus vertical lines; auditory: low versus high pitch tones) from stimulus-locked data (Fig B in S1 Text); decoding of response information from stimulus-locked data (Fig C in S1 Text, panels A and B). We performed a supplementary temporal generalization analysis [20] to probe whether the multivariate codes underlying the 2 peak deflections in the response decoding time course were representationally distinct (Fig C in S1 Text, panel C). We also conducted network decoding of response information using an alternative method that confined MVPA to more "unique" signals for each network (Fig D in S1 Text), which revealed a highly similar pattern of results.

MVAR estimation of restFC: Rationale

The source-modeled rest EEG data were used to estimate the lagged FC weights (Fig 3A) that parameterized the dynamic activity flow model (Fig 3B). Note that we only used the pre-task rest phase here (see Participants and study design section), given the potential for influences of the task on FC in the post-task rest phase. These could encompass second-order connectivity changes induced by the task [109] or first-order coactivation effects from cognitive replay of the task [110], which could have introduced circularity in predicting activation/information in the earlier task phase.

Our motivations for using a MVAR FC approach stemmed from the overarching aim of imposing certain constraints on the subsequent dynamic activity flow modeling, taking inspiration from concepts in the causal inference [49] and causal connectivity [50,51] literatures. Note that by imposing these modeling constraints, we do not claim to have effectively solved the problem of identifying causal relationships between brain regions. Rather, we took these steps as a principled means to reduce the available space of inquiry and improve (in a relative sense) the likelihood of identifying true causal relationships in the brain via our adopted MVAR FC approach compared to other less constrained methods (e.g., Pearson correlation, univariate/bivariate autoregressive modeling). We have delved into these concepts in detail in prior theoretical work [32,69].

For the first of these principled reduction steps, MVAR permits estimation of dynamic aspects of FC through the inclusion of predictors over temporally lagged time points [73,111], in contradistinction from static FC methods (e.g., Pearson correlation or multiple linear regression estimated over an entire rest session). Secondly, our MVAR approach allows for separation of contemporaneous (connectivity of region A at t0 with region B at t0) and lagged (connectivity of region A at t0-1 lag with region B at t0) contributions to FC [72,112]. This is unlike typical sliding window dynamic FC approaches, which assess fluctuations in contemporaneous influences over discrete time windows [113], and have been criticized for potentially capturing sampling variability (i.e., noisy estimates of static FC) rather than true dynamic interactions [73,114]. Our emphasis on the "lagged" nature of our approach is predicated on modeling both contemporaneous and lagged terms in the MVAR model so as to estimate the true lagged FC effects. This differentiates our approach from alternative autoregressive methods that also target dynamic FC influences by modeling lags, but do so without accounting for contemporaneous ones (leading to errors in lag estimation, as previously reported; [72]). Estimation of dynamic FC with clear separation of lagged influences was essential to our goal of predicting future activation/information states via dynamic activity flow modeling.

Third, our MVAR approach fitted all spatial ("source" predictor regions) and temporal (t0-n lags) terms simultaneously via multiple linear regression models (Fig 3A), meaning that the approach is fully multivariate in both the temporal and spatial domains. This reduces the impact of indirect spatial or temporal influences from serving as unobserved confounders on the FC weights, which would likely arise to a greater extent if alternative bivariate FC estimation methods were used [49,69,115], or if alternative neuroimaging modalities were used (e.g., the poor temporal resolution of fMRI allowing for temporal confounding, and the poor whole-brain coverage of animal electrophysiology allowing for spatial confounding). Whereas the risk of unobserved confounders still persists [116], as do related problems introduced by source EEG data (e.g., the coarse spatial scale of EEG, field spread artifacts), we have at least reduced this risk by adopting a multivariate rather than univariate approach to restFC estimation and network modeling. Fourth, our exclusive focus on the lagged MVAR estimates for dynamic activity flow modeling (see later Methods section for details) imparted directionality to the approach, given that past t0-n lagged terms predicted future target t0 terms (Fig 3B). This autoregressive form of directionality is the basis of Granger Causality methods [65,117], which have been fruitfully applied to both fMRI and source modeled MEG/EEG data [74,118,119].

To summarize, each of the 4 terms we use to describe our approach is intended to clarify a principled constraint versus alternative approaches: dynamic (versus static), lagged (estimating both lagged and contemporaneous effects, versus the lags alone), direct (multivariate in spatial and time domains, versus univariate) and directional (modeling future activity from the past lagged terms versus modeling them from lagged and contemporaneous ones). MVAR yielded FC estimates that hence increased the overall validity—according to extant causal inference/connectivity frameworks [32,69]—of this version of activity flow modeling beyond previous versions.

MVAR estimation of restFC: Specific approach

The rest data (already segmented into 20 s nonoverlapping pseudo-trials; see EEG preprocessing section) were firstly downsampled from 1000 Hz to 200 Hz. This matched the downsampling applied to the task data and reduced computation time for the intensive MVAR procedure. Note that we selected 20 s as the length of each pseudo-trial to capture the lower bound of the low frequency fluctuations considered to contribute to resting-state FC (i.e., 0.1 to 1 Hz, with 20 s allowing 2 cycles of 10 s; 120, 121), as well as contributions from higher frequencies.

Consistent with our focus on predicting activation/information states in the Motor network via dynamic activity flow modeling (see next section), the multiple linear regression models comprising the MVAR step treated the 35 Motor network regions as to-be-predicted (target, j in Fig 3A) regions, and the remaining network regions as predictor (source, i) regions. Time series for all regions were firstly z-scored within each pseudo-trial. A model order of 10 lags was selected (i.e., t0-10 time points extending 50ms into the past of each target t0 time point), based on evidence from invasive electrophysiology suggesting 50 to 100 ms as a reasonable timescale over which task information fluctuates [13,122,123], and our previous work directly involving autoregressive modeling in EEG/MEG data that used these parameters [74,124]. We opted for the lower bound of this range (50 ms) given the computationally intensive nature of regularized MVAR restFC estimation (3 to 5 days runtime per participant), which scaled with the number of predictors entered in the PCA autoregression model and hence increased with larger model orders. As a control analysis, we also present dynamic activity flow model accuracy results across variation in model order (25 ms and 75 ms; see Results, Fig 8C).

When selecting MVAR predictor terms, our general approach was to estimate all possible spatial and temporal terms to eliminate indirect influences arising from unobserved confounders, with more selective use of predictors in the later dynamic activity flow modeling step. Hence, all non-target Motor network regions were included in the MVAR source set, despite these regions being excluded from dynamic activity flow (to focus the model on long-distance connections, see next section). Similarly, both contemporaneous (t0) and lagged (t0-10 lags) terms were included for source predictor regions during the MVAR step, despite basing the dynamic activity flow modeling solely on the lagged source terms (to preserve our aim of predicting future activation/information states). This follows previous simulation work demonstrating that inclusion of contemporaneous terms improves the precision of lagged estimates, versus fitting the lagged terms alone [72]. The MVAR models for each target region also included a set of autoregressive lagged terms (over t0-10, excluding t0 to prevent circularity) that estimated serial autocorrelation or self-coupling as per common guidelines [72,73,117].

The MVAR FC weights for the input spatial and temporal terms were estimated via a regularized form of multiple linear regression, involving PCA (Fig 3A). We have applied a nonautoregressive variant of this FC approach recently [31], and the regularization here was similarly focused on identifying the number of predictor PCs (nPCs) included in each MVAR regression that would reduce overfitting to noise. The approach employs cross-validation to identify the optimal number of principal components to include in regression models estimated for each participant, so as to regularize the output FC beta coefficients and minimize overfitting. To ensure tractability during this computationally intensive procedure, nPCs were varied from 1 to the max number of PCs (i.e., the rank of the predictors, approximately 2,700) in increments of 540. Hence, for a given Motor target region on a given rest pseudo-trial, PCA was run on the accompanying predictor matrix (263 contemporaneous source + 263*10 lagged source + 10 lagged self-coupling terms = 2,903 predictors, fit to each 20 s pseudo-trial of 4,000 observations). The nPCs retained were varied as per the regularization (1:540:max), with the target region's time series then regressed onto those selected nPC scores. The resulting beta weights were transformed back to the original predictor space, and then applied to predict the target time series for the next pseudo-trial. The MSE between the actual and predicted next-pseudo-trial time series was stored, with this process repeated for all trials in sequence (i.e., train on pseudo-trial1, test on pseudo-trial2; train on pseudo-trial2, test on pseudo-trial3 etc). Note that this corresponds to a "sliding window" cross-validation scheme that preserves the serial ordering of the input time series during model training (unlike more general k-fold cross-validation schemes) to theoretically improve generalization [125]. The full regularization scheme hence generated an MSE output variable with dimensions nPCs × target regions × test

pseudo-trials, with the optimal nPCs finally selected as that yielding the minimal MSE (averaged across target regions and test pseudo-trials) for that participant. This optimal nPC value was used to estimate the final MVAR restFC weights for all Motor network targets across all pseudo-trials for that participant, with the cross-pseudo-trial average restFC matrix used in the next dynamic activity flow modeling step.

Dynamic activity flow modeling

We applied dynamic activity flow modeling to capture the emergence of future response information representations in the Motor network. The model is depicted graphically in Fig 3B and summarized in the following equation:

$$Y_t = \sum_{i=1}^{10} X_{t-i} F_{t-i} + \sum_{i=1}^{10} Y_{t-i} C_{t-i},$$

where t represents a future to-be-predicted task trial time point, i the set of lagged time points extending 10 time points into the past, Y the to-be-predicted regional activation (and lagged autoregressive terms on the right of the equation), X represents the lagged source (non-Motor network) predictor regional activations, F represents the lagged source predictor restFC terms, and C represents the lagged autoregressive/self-coupling restFC terms.

The present model built on previous versions [16,30,31] by including stronger modeling constraints. As introduced in the previous MVAR FC estimation sections, these constraints ensured that predictions of future response information states were made from activity flowing over functional network connections in a dynamic, lagged, direct, and directional fashion. This more principled grounding was strengthened by focusing the modeling on response information representations, given that these underlie generation of overt behavior and hence likely mark a causal end-point of cognitive task processing [21,67]. This justified imposing directionality from t0-n lagged non-Motor sources→t0 Motor targets in the model (Fig 3B). Such temporal directionality would be harder to ascribe in dynamic activity flow models of sensory information in the Visual network (following up on the sensory decoding results; see Fig A in S1 Text), given greater alternation between feedforward (activity flow from lagged non-Visual sources→Visual targets) and feedback cycles (lagged Visual sources→non-Visual targets; [18]).

To reiterate, certain predictor terms that were modeled in the MVAR restFC step were excluded from the ensuing dynamic activity flow modeling: non-target Motor regions and contemporaneous (t0) source terms. These exclusions focused the predictions on spatially long-range and temporally in-the-future activity flow processes respectively. Lagged autoregressive terms were included to account for local self-coupling processes that likely contribute to dynamic activity flow. The source-modeled task EEG data were firstly downsampled to 200 Hz. Predicted activations for each target Motor network region (j in Fig 3B), for each task trial, for each time point (t0), were then generated from the dot product of lagged task activations (for sources and self-coupling terms, over the same model order of t0-10 samples) and lagged rest MVAR restFC weights (capturing FC from the sources and self-coupling terms *to* the targets). This generated a matrix of predicted Motor region task activations with the same dimensions (Motor regions × task trials × time points) as the actual task activations used for the previous decoding analyses. This predicted activation matrix was the basis of subsequent assessments of model accuracy: response information decoded via dynamic MVPA, motor ERP analyses and representational overlap (see ensuing sections).

Some further features of the model that aimed to rigorously rule out circularity are worth highlighting. To reiterate, causal filtering was used during preprocessing to prevent introduction of circularity due to temporal leakage (i.e., task activation from targets at t0 leaking to

lagged predictors after filtering; see earlier Methods section). Note also that the MVAR FC weights were derived from a resting-state session that was entirely separate from the task activation data, which prevented circularity in estimating FC from the same task session as the to-be-predicted data (due to first-order task coactivation effects contaminating the FC weights; 110). We also implemented multiple strategies to mitigate circularity introduced by EEG field spread artifacts, which could lead to target t0 activations spreading to spatially proximal predictor regions. First, we employed beamformer source modeling, which has been shown to minimize such artifacts compared to alternative methods (see EEG source modeling section; 33). Our use of the Power functional atlas [43] to identify source regions also helped with this goal, given that each region is spaced at least 10 mm apart from each other and hence avoids the most severe field spread arising between highly proximal regions [33]. Our exclusion of the contemporaneous (t0) source terms from the activity flow step also mitigates field spread, as these artifacts are instantaneous and hence unlikely to influence lagged terms [34,126]. Our careful use of causal filters as highlighted above eliminated any residual possibility of field spread-related signals leaking from a target time point t0 to lagged time points in the past. As a final rigorous control, we also regressed out the task time series for a given target (t0) from all predictor source regions (at the same t0), prior to rearranging them into lagged predictors for dynamic activity flow modeling. This regression step was run just prior to all dynamic activity flow modeling analyses presented in the main manuscript and effectively removed all contemporaneous influences (including those resulting from field spread and temporal leakage of information) on the model outputs. The supplement describes how this step actually numerically improved the model prediction accuracy (versus omission of this step; Fig G in S1 Text).

Assessment of dynamic activity flow model accuracy: Dynamic MVPA

The accuracy of dynamic activity flow modeling was assessed in a number of ways (Fig 3B). Our primary approach was to apply the identical dynamic MVPA procedure to the model-predicted Motor region activation time series as was applied to the actual data (see Dynamic MVPA section). This yielded a predicted response information time course, for which significant decodability at each time point was assessed via Wilcoxon sign rank against 50% chance (Bonferroni corrected across multiple time point comparisons, as before). The recovery of significantly decodable time points in the predicted time course would provide evidence that our dynamic activity flow modeling approach accurately captured the emergence of future response information. The success of the model in capturing the temporal morphology of the response information time course was also quantified via Pearson correlation of the predicted and actual time courses. This was computed both after averaging the time courses across participants (group-level overlap), as well as with a random effects approach that correlated the predicted and actual time courses for each participant and contrasted this r value (after Fisher-z transform) against 0 via 1-sample *t* test (subject-level overlap).

We also report the coefficient of determination (R^2) computed using the sum of squares formulation (108) for all dynamic activity flow models. This metric permits assessment of scaled prediction accuracy (unlike Pearson r), as well as providing insight into whether the model predictions outperform those based on the average actual data. To quantify whether R^2 was reliably greater than 0 (indicating that dynamic activity flow modeling outperformed the average model), we adapted the random effects approach used for the Pearson r metrics: computing R^2 for each participants' predicted/actual data, and contrasting at the group level against 0 via 1-sample *t* test. For the dynamic MVPA analysis, we also conducted a permutation testing analysis to further highlight the prediction accuracy of our model. This is described in the Results.

Assessment of dynamic activity flow model accuracy: Motor ERP

We also examined the model's accuracy in capturing the activations in Motor network regions that underpinned the dynamic MVPA analyses. This targeted recovery of the well-established motor ERP termed the lateralized readiness potential [52–54]. This reflects greater activation around response commission in the Motor network hemisphere contralateral to the response hand. For each participant, the model-predicted trial activations were arranged into "contralateral" (left-response for right hemisphere regions and right-response for left hemisphere regions) and "ipsilateral" (left-response for left hemisphere and right-response for right hemisphere) conditions and averaged across regions and trials. The difference wave for the resulting contralateral minus ipsilateral waveforms hence indexed recovery of the motor ERP for each participant, with this entire process applied separately to the model-predicted and actual data. In both predicted/actual cases, significance was assessed by contrasting the participant motor ERP fluctuations at each time point against 0 via Wilcoxon sign rank test, with Bonferroni correction for multiple time point comparisons.

The accuracy of the model in predicting the raw task activation effects was assessed firstly as the ability to recover significant activations in the predicted motor ERP waveform. We also quantified the model's ability to recover the morphology of the motor ERP by correlating the predicted and actual difference waves, at both the group and subject levels. While this constituted an assessment of "temporal overlap," we were also able to probe predicted-to-actual overlap in the spatial domain as the ERP analyses did not aggregate information across spatially distinct regions (i.e were spatially univariate unlike the dynamic MVPA analyses). The participant motor ERPs were averaged over significant epochs identified in the group actual waveform, separately for each Motor region, and separately for the predicted and actual data. The predicted and actual activation vectors were then correlated at the group and subject levels to interrogate how well the dynamic activity flow model captured the spatial pattern of Motor network activations. To ensure that spatial overlap was not critically dependent on the selected significant epoch, we also assessed group- and subject-level overlap between predicted and actual activation vectors that concatenated all Motor regions and all trial time points (i.e., capturing the degree of "spatiotemporal overlap" across the entire trial time course).

Assessment of dynamic activity flow model accuracy: Representational overlap

We also probed the extent to which the multivariate representations underlying the accurate decoding of response information in the activity flow-predicted data overlapped with the representations in the actual data. Such direct "representational overlap" between the predicted and actual data would increase confidence that dynamic activity flow modeling is capturing how the brain veridically represents response information. To address this, we tested whether response information in the actual data could be decoded from multivariate representations trained in the predicted data. This approach of training in the predicted and testing in the actual data is in contrast to that adopted in the main decoding analysis (Fig 6A), wherein training and testing was performed in the predicted data. We employed a method inspired by representational similarity analysis [16,127,128], which was capable of more fine-grained assessment of the similarity in representational geometry (by computing continuous Pearson r similarity values as the measure of classification accuracy) than the SVM classification approach used for the main dynamic MVPA analyses (which output categorical decisions to assess accuracy).

Predicted task activations for Motor regions were generated via dynamic activity flow modeling as described above, which were then averaged into subtrials separately for the 2 response conditions (correct left and correct right) and assigned into training and test sets via

10-fold cross-validation (as with the dynamic MVPA analyses). Representational templates were created at each time point for each response condition by averaging Motor region activations over relevant trial indices in the predicted data. These time point-by-time point predicted representations were then applied to decode the actual Motor activations in the held-out test trials. For each time point in each test trial, Pearson correlations were computed between the actual activation vector and both the "correct" predicted condition template (e.g., left response template correlated with actual left response test trial) and the "incorrect" predicted condition template (e.g., right response template correlated with actual left response test trial). Hence, the difference value for correct r minus incorrect r provided an estimate of response information decodability at each time point in the actual test data (with values > 0 denoting presence of information). Iterating this process over all time points, testing folds and subtrial iterations for each participant generated a time course capturing the degree of overlap between the predicted and actual response information representations.

Statistical significance of the representational time course was again examined via Wilcoxon sign rank tests against 0, with Bonferroni correction across multiple time point comparisons. Recovery of significantly decodable time points in this "TrainPred-TestActual" time course provided evidence that the dynamic activity flow model accurately captured representations underlying future information decoding in the actual data. For comparison, we repeated the same representational similarity approach with trained condition templates computed in the actual data, thereby generating a "TrainActual-TestActual" time course. Correlating the TrainPred-TestActual and TrainActual-TestActual time courses (at both the group and subject levels) hence clarified how well the activity flow model captured dynamics in representational geometry over the entire trial.

Network lesioning extension of dynamic activity flow modeling

To extend the dynamic activity flow model toward insight into principles of functional brain organization, we applied a modified "network lesioning" variant of the model. This followed a similar approach to generating activity flow-predicted response information time courses for the Motor network via dynamic MVPA, as described above. The critical difference here was that information time courses were predicted via separate activity flow models that selectively "lesioned" all except one of the 11 functional networks from the Power atlas. Hence, only regions within one specific network were included in the predictor source set (Fig 3B) for each dynamic activity flow model, with lagged self-coupling/autoregressive terms also excluded. This yielded 10 time courses capturing the unique contributions to response information decoding made by each individual network. Comparing peak decodability across network models hence provided more computational insight into which networks were dominant drivers of response information. Such comparisons were made via visual inspection of the 10 lesioned information time courses, as well as by contrasting decoding peaks (extracted for each participant from the group time-to-peak across networks) via paired Wilcoxon sign rank tests (with FDR correction for multiple pairwise network comparisons). As an alternative to contrasting peak decoding accuracies, we also contrasted the subject-level prediction accuracy for each network model (i.e., Pearson r for each network-predicted time course with the actual Motor network time course) via paired Wilcoxon sign rank tests (with FDR correction for multiple pairwise network comparisons). This captured how well each lesioned network model predicted the morphology of the actual response information time course (Fig H in S1 Text).

Supporting information

S1 Text. Document detailing all Supporting information analyses and accompanying figures.
(DOCX)

Acknowledgments

The authors acknowledge the Office of Advanced Research Computing (OARC) at Rutgers, The State University of New Jersey for providing access to the Amarel cluster and associated research computing resources that have contributed to the results reported here. The authors thank Dr. Bart Krekelberg for providing access to the EEG equipment used to collect data for this report, which was purchased with funding secured by Dr. Krekelberg from the US National Science Foundation. We also thank Jasmine Siegel for assisting during installing and collecting data using this equipment.

Author Contributions

Conceptualization: Ravi D. Mill, Michael W. Cole.

Data curation: Ravi D. Mill, Julia L. Hamilton, Emily C. Winfield, Nicole Lalta, Richard H. Chen.

Formal analysis: Ravi D. Mill.

Funding acquisition: Michael W. Cole.

Investigation: Ravi D. Mill, Michael W. Cole.

Methodology: Ravi D. Mill, Michael W. Cole.

Project administration: Julia L. Hamilton, Emily C. Winfield, Nicole Lalta, Richard H. Chen.

Resources: Ravi D. Mill, Michael W. Cole.

Software: Ravi D. Mill, Michael W. Cole.

Supervision: Ravi D. Mill, Michael W. Cole.

Validation: Ravi D. Mill, Julia L. Hamilton, Michael W. Cole.

Visualization: Ravi D. Mill.

Writing – original draft: Ravi D. Mill, Michael W. Cole.

Writing – review & editing: Ravi D. Mill, Julia L. Hamilton, Emily C. Winfield, Nicole Lalta, Richard H. Chen, Michael W. Cole.

References

1. Haynes JD. A Primer on Pattern-Based Approaches to fMRI: Principles, Pitfalls, and Perspectives. Neuron. 2015 Jul; 87(2):257–70. https://doi.org/10.1016/j.neuron.2015.05.025 PMID: 26182413
2. Kriegeskorte N, Kievit RA. Representational geometry: integrating cognition, computation, and the brain. Trends Cogn Sci. 2013 Aug; 17(8):401–12. https://doi.org/10.1016/j.tics.2013.06.007 PMID: 23876494
3. Kriegeskorte N, Mur M, Ruff DA, Kiani R, Bodurka J, Esteky H, et al. Matching Categorical Object Representations in Inferior Temporal Cortex of Man and Monkey. Neuron. 2008 Dec; 60(6):1126–41. https://doi.org/10.1016/j.neuron.2008.10.043 PMID: 19109916
4. Grootswagers T, Wardle SG, Carlson TA. Decoding Dynamic Brain Patterns from Evoked Responses: A Tutorial on Multivariate Pattern Analysis Applied to Time Series Neuroimaging Data. J Cogn Neurosci. 2017 Apr; 29(4):677–97. https://doi.org/10.1162/jocn_a_01068 PMID: 27779910
5. Jimura K, Poldrack RA. Analyses of regional-average activation and multivoxel pattern information tell complementary stories. Neuropsychologia. 2012 Mar; 50(4):544–52. https://doi.org/10.1016/j.neuropsychologia.2011.11.007 PMID: 22100534
6. Kriegeskorte N, Goebel R, Bandettini P. Information-based functional brain mapping. Proc Natl Acad Sci. 2006 Mar 7; 103(10):3863–8. https://doi.org/10.1073/pnas.0600244103 PMID: 16537458

7. Saxena S, Cunningham JP. Towards the neural population doctrine. Curr Opin Neurobiol. 2019 Apr; 55:103–11. https://doi.org/10.1016/j.conb.2019.02.002 PMID: 30877963

8. Eichenbaum H. Barlow versus Hebb: When is it time to abandon the notion of feature detectors and adopt the cell assembly as the unit of cognition? Neurosci Lett. 2018 Jul; 680:88–93. https://doi.org/10.1016/j.neulet.2017.04.006 PMID: 28389238

9. Bernardi S, Benna MK, Rigotti M, Munuera J, Fusi S, Salzman CD. The Geometry of Abstraction in the Hippocampus and Prefrontal Cortex. Cell. 2020; 183 (4):954 –967.e21. https://doi.org/10.1016/j.cell.2020.09.031 PMID: 33058757

10. Kauvar IV, Machado TA, Yuen E, Kochalka J, Choi M, Allen WE, et al. Cortical Observation by Synchronous Multifocal Optical Sampling Reveals Widespread Population Encoding of Actions. Neuron. 2020 Jul; 107(2):351–367.e19. https://doi.org/10.1016/j.neuron.2020.04.023 PMID: 32433908

11. Raposo D, Kaufman MT, Churchland AK. A category-free neural population supports evolving demands during decision-making. Nat Neurosci. 2014 Dec; 17(12):1784–92. https://doi.org/10.1038/nn.3865 PMID: 25383902

12. Rigotti M, Barak O, Warden MR, Wang XJ, Daw ND, Miller EK, et al. The importance of mixed selectivity in complex cognitive tasks. Nature. 2013 May; 497(7451):585–90. https://doi.org/10.1038/nature12160 PMID: 23685452

13. Siegel M, Buschman TJ, Miller EK. Cortical information flow during flexible sensorimotor decisions. Science. 2015 Jun 19; 348(6241):1352–5. https://doi.org/10.1126/science.aab0551 PMID: 26089513

14. Hernández A, Nácher V, Luna R, Zainos A, Lemus L, Alvarez M, et al. Decoding a Perceptual Decision Process across Cortex. Neuron. 2010 Apr; 66(2):300–14. https://doi.org/10.1016/j.neuron.2010.03.031 PMID: 20435005

15. Cole MW, Ito T, Braver TS. The Behavioral Relevance of Task Information in Human Prefrontal Cortex. Cereb Cortex. 2016 Jun; 26(6):2497–505. https://doi.org/10.1093/cercor/bhv072 PMID: 25870233

16. Ito T, Kulkarni KR, Schultz DH, Mill RD, Chen RH, Solomyak LI, et al. Cognitive task information is transferred between brain regions via resting-state network topology. Nat Commun [Internet] 2017 Dec [cited 2018 Nov 4]; 8(1). Available from: http://www.nature.com/articles/s41467-017-01000-w. https://doi.org/10.1038/s41467-017-01000-w PMID: 29044112

17. Zhang J, Kriegeskorte N, Carlin JD, Rowe JB. Choosing the Rules: Distinct and Overlapping Frontoparietal Representations of Task Rules for Perceptual Decisions. J Neurosci 2013 Jul 17; 33 (29):11852–62. https://doi.org/10.1523/JNEUROSCI.5193-12.2013 PMID: 23864675

18. Gwilliams L, King JR. Recurrent processes support a cascade of hierarchical decisions. eLife [Internet]. 2020 Sep 1 [cited 2020 Oct 13]; 9. Available from: https://elifesciences.org/articles/56603. https://doi.org/10.7554/eLife.56603 PMID: 32869746

19. Hubbard J, Kikumoto A, Mayr U. EEG Decoding Reveals the Strength and Temporal Dynamics of Goal-Relevant Representations. Sci Rep [Internet]. 2019 Dec [cited 2020 Dec 19]; 9(1). Available from: http://www.nature.com/articles/s41598-019-45333-6. https://doi.org/10.1038/s41598-019-45333-6 PMID: 31227796

20. King JR, Dehaene S. Characterizing the dynamics of mental representations: the temporal generalization method. Trends Cogn Sci. 2014 Apr; 18(4):203–10. https://doi.org/10.1016/j.tics.2014.01.002 PMID: 24593982

21. de-Wit L, Alexander D, Ekroll V, Wagemans J. Is neuroimaging measuring information in the brain? Psychon Bull Rev. 2016 Oct; 23(5):1415–28. https://doi.org/10.3758/s13423-016-1002-0 PMID: 26833316

22. Ito T, Hearne L, Mill R, Cocuzza C, Cole MW. Discovering the Computational Relevance of Brain Network Organization. Trends Cogn Sci. 2019 Nov;S1364661319302402. https://doi.org/10.1016/j.tics.2019.10.005 PMID: 31727507

23. Hebb DO. The organization of behavior: a neuropsychological theory. Mahwah, N.J: L. Erlbaum Associates; 1949.

24. Levy WB, Steward O. Temporal contiguity requirements for long-term associative potentiation/depression in the hippocampus. Neuroscience. 1983 Apr; 8(4):791–7. https://doi.org/10.1016/0306-4522(83)90010-6 PMID: 6306504

25. Caporale N, Dan Y. Spike Timing–Dependent Plasticity: A Hebbian Learning Rule. Annu Rev Neurosci. 2008 Jul; 31(1):25–46. https://doi.org/10.1146/annurev.neuro.31.060407.125639 PMID: 18275283

26. Petersen SE, Sporns O. Brain Networks and Cognitive Architectures. Neuron. 2015 Oct; 88(1):207–19. https://doi.org/10.1016/j.neuron.2015.09.027 PMID: 26447582

27. Wig GS, Schlaggar BL, Petersen SE. Concepts and principles in the analysis of brain networks: Brain networks. Ann N Y Acad Sci. 2011 Apr; 1224(1):126–46. https://doi.org/10.1111/j.1749-6632.2010.05947.x PMID: 21486299

28. Lewis CM, Baldassarre A, Committeri G, Romani GL, Corbetta M. Learning sculpts the spontaneous activity of the resting human brain. Proc Natl Acad Sci. 2009 Oct 13; 106(41):17558–63. https://doi.org/10.1073/pnas.0902455106 PMID: 19805061

29. Newbold DJ, Laumann TO, Hoyt CR, Hampton JM, Montez DF, Raut RV, et al. Plasticity and Spontaneous Activity Pulses in Disused Human Brain Circuits. Neuron. 2020 Aug; 107(3):580–589.e6. https://doi.org/10.1016/j.neuron.2020.05.007 PMID: 32778224

30. Cole MW, Ito T, Bassett DS, Schultz DH. Activity flow over resting-state networks shapes cognitive task activations. Nat Neurosci. 2016 Dec; 19(12):1718–26. https://doi.org/10.1038/nn.4406 PMID: 27723746

31. Mill RD, Gordon BA, Balota DA, Cole MW. Predicting dysfunctional age-related task activations from resting-state network alterations. Neuroimage. 2020; 221:117167. https://doi.org/10.1016/j.neuroimage.2020.117167 PMID: 32682094

32. Mill RD, Ito T, Cole MW. From connectome to cognition: The search for mechanism in human functional brain networks. Neuroimage. 2017 Oct; 160:124–39. https://doi.org/10.1016/j.neuroimage.2017.01.060 PMID: 28131891

33. Schoffelen JM, Gross J. Source connectivity analysis with MEG and EEG. Hum Brain Mapp. 2009 Jun; 30(6):1857–65. https://doi.org/10.1002/hbm.20745 PMID: 19235884

34. Stinstra JG, Peters MJ. The volume conductor may act as a temporal filter on the ECG and EEG. Med Biol Eng Comput. 1998; 36 (6):711–6. https://doi.org/10.1007/BF02518873 PMID: 10367461

35. Buonomano D, Merzenich M. Temporal information transformed into a spatial code by a neural network with realistic properties. Science. 1995 Feb 17; 267(5200):1028–30. https://doi.org/10.1126/science.7863330 PMID: 7863330

36. Eliasmith C, Stewart TC, Choo X, Bekolay T, DeWolf T, Tang Y, et al. A Large-Scale Model of the Functioning Brain. Science. 2012 Nov 30; 338(6111):1202–5. https://doi.org/10.1126/science.1225266 PMID: 23197532

37. Yamins DLK, Hong H, Cadieu CF, Solomon EA, Seibert D, DiCarlo JJ. Performance-optimized hierarchical models predict neural responses in higher visual cortex. Proc Natl Acad Sci. 2014 Jun 10; 111 (23):8619–24. https://doi.org/10.1073/pnas.1403112111 PMID: 24812127

38. Sinz FH, Pitkow X, Reimer J, Bethge M, Tolias AS. Engineering a Less Artificial Intelligence. Neuron. 2019 Sep; 103(6):967–79. https://doi.org/10.1016/j.neuron.2019.08.034 PMID: 31557461

39. Kriegeskorte N, Douglas PK. Cognitive computational neuroscience. Nat Neurosci. 2018 Sep; 21 (9):1148–60. https://doi.org/10.1038/s41593-018-0210-5 PMID: 30127428

40. Brookes MJ, Mullinger KJ, Stevenson CM, Morris PG, Bowtell R. Simultaneous EEG source localisation and artifact rejection during concurrent fMRI by means of spatial filtering. Neuroimage. 2008 Apr; 40(3):1090–104. https://doi.org/10.1016/j.neuroimage.2007.12.030 PMID: 18296069

41. Hui HB, Pantazis D, Bressler SL, Leahy RM. Identifying true cortical interactions in MEG using the nulling beamformer. Neuroimage. 2010 Feb; 49(4):3161–74. https://doi.org/10.1016/j.neuroimage.2009.10.078 PMID: 19896541

42. Van Veen BD, Van Drongelen W, Yuchtman M, Suzuki A. Localization of brain electrical activity via linearly constrained minimum variance spatial filtering. IEEE Trans Biomed Eng. 1997 Sep; 44(9):867–80. https://doi.org/10.1109/10.623056 PMID: 9282479

43. Power JD, Cohen AL, Nelson SM, Wig GS, Barnes KA, Church JA, et al. Functional Network Organization of the Human Brain. Neuron. 2011; 72 (4):665–78. https://doi.org/10.1016/j.neuron.2011.09.006 PMID: 22099467

44. Klamer S, Elshahabi A, Lerche H, Braun C, Erb M, Scheffler K, et al. Differences Between MEG and High-Density EEG Source Localizations Using a Distributed Source Model in Comparison to fMRI. Brain Topogr. 2015 Jan; 28(1):87–94. https://doi.org/10.1007/s10548-014-0405-3 PMID: 25296614

45. Lascano AM, Grouiller F, Genetti M, Spinelli L, Seeck M, Schaller K, et al. Surgically Relevant Localization of the Central Sulcus With High-Density Somatosensory-Evoked Potentials Compared With Functional Magnetic Resonance Imaging. Neurosurgery. 2014 May 1; 74(5):517–26. https://doi.org/10.1227/NEU.0000000000000298 PMID: 24463494

46. Seeber M, Cantonas LM, Hoevels M, Sesia T, Visser-Vandewalle V, Michel CM. Subcortical electrophysiological activity is detectable with high-density EEG source imaging. Nat Commun. 2019 Dec; 10(1):753. https://doi.org/10.1038/s41467-019-08725-w PMID: 30765707

47. Elsayed GF, Lara AH, Kaufman MT, Churchland MM, Cunningham JP. Reorganization between preparatory and movement population responses in motor cortex. Nat Commun [Internet] 2016 Dec [cited

2020 Oct 21]; 7(1). Available from: http://www.nature.com/articles/ncomms13239. https://doi.org/10.1038/ncomms13239 PMID: 27807345

48. Wascher E, Wauschkuhn B. The interaction of stimulus- and response-related processes measured by event-related lateralizations of the EEG. Electroencephalogr Clin Neurophysiol. 1996 Aug; 99 (2):149–62. https://doi.org/10.1016/0013-4694(96)95602-3 PMID: 8761051

49. Pearl J, Mackenzie D. The book of why: the new science of cause and effect. First edition. New York: Basic Books; 2018. 418 p.

50. Mumford JA, Ramsey JD. Bayesian networks for fMRI: A primer. Neuroimage. 2014 Feb; 86:573–82. https://doi.org/10.1016/j.neuroimage.2013.10.020 PMID: 24140939

51. Ramsey JD, Hanson SJ, Hanson C, Halchenko YO, Poldrack RA, Glymour C. Six problems for causal inference from fMRI. Neuroimage. 2010 Jan; 49(2):1545–58. https://doi.org/10.1016/j.neuroimage.2009.08.065 PMID: 19747552

52. Cheyne D, Bakhtazad L, Gaetz W. Spatiotemporal mapping of cortical activity accompanying voluntary movements using an event-related beamforming approach. Hum Brain Mapp. 2006 Mar; 27 (3):213–29. https://doi.org/10.1002/hbm.20178 PMID: 16037985

53. Deecke L, Grozinger B, Kornhuber HH. Voluntary finger movement in man: Cerebral potentials and theory. Biol Cybern. 1976; 23 (2):99–119. https://doi.org/10.1007/BF00336013 PMID: 949512

54. Kutas M, Donchin E. Preparation to respond as manifested by movement-related brain potentials. Brain Res. 1980; 202 (1):95–115. PMID: 7427748

55. Yamins DLK, DiCarlo JJ. Using goal-driven deep learning models to understand sensory cortex. Nat Neurosci. 2016 Mar; 19(3):356–65. https://doi.org/10.1038/nn.4244 PMID: 26906502

56. Yang GR, Wang XJ. Artificial Neural Networks for Neuroscientists: A Primer. Neuron. 2020 Sep; 107 (6):1048–70. https://doi.org/10.1016/j.neuron.2020.09.005 PMID: 32970997

57. Penny WD, Stephan KE, Mechelli A, Friston KJ. Comparing dynamic causal models. Neuroimage. 2004 Jul; 22(3):1157–72. https://doi.org/10.1016/j.neuroimage.2004.03.026 PMID: 15219588

58. Hassan M, Dufor O, Merlet I, Berrou C, Wendling F. EEG Source Connectivity Analysis: From Dense Array Recordings to Brain Networks. D'Ausilio A, editor. PLoS ONE. 2014 Aug 12; 9(8):e105041. https://doi.org/10.1371/journal.pone.0105041 PMID: 25115932

59. Song J, Davey C, Poulsen C, Luu P, Turovets S, Anderson E, et al. EEG source localization: Sensor density and head surface coverage. J Neurosci Methods. 2015 Dec; 256:9–21. https://doi.org/10.1016/j.jneumeth.2015.08.015 PMID: 26300183

60. Vorwerk J, Oostenveld R, Piastra MC, Magyari L, Wolters CH. The FieldTrip-SimBio pipeline for EEG forward solutions. Biomed Eng OnLine [Internet]. 2018 Dec [cited 2020 Jun 14]; 17(1). Available from: https://biomedical-engineering-online.biomedcentral.com/articles/10.1186/s12938-018-0463-y. https://doi.org/10.1186/s12938-018-0463-y PMID: 29580236

61. Haufe S, Nikulin VV, Müller KR, Nolte G. A critical assessment of connectivity measures for EEG data: A simulation study. Neuroimage. 2013 Jan; 64:120–33. https://doi.org/10.1016/j.neuroimage.2012.09.036 PMID: 23006806

62. Van de Steen F, Faes L, Karahan E, Songsiri J, Valdes-Sosa PA, Marinazzo D. Critical Comments on EEG Sensor Space Dynamical Connectivity Analysis. Brain Topogr. 2019 Jul; 32(4):643–54. https://doi.org/10.1007/s10548-016-0538-7 PMID: 27905073

63. Ames KC, Ryu SI, Shenoy KV. Simultaneous motor preparation and execution in a last-moment reach correction task. Nat Commun [Internet]. 2019 Dec [cited 2020 Oct 22]; 10(1). Available from: http://www.nature.com/articles/s41467-019-10772-2.

64. Hanks TD, Kopec CD, Brunton BW, Duan CA, Erlich JC, Brody CD. Distinct relationships of parietal and prefrontal cortices to evidence accumulation. Nature. 2015 Apr; 520(7546):220–3. https://doi.org/10.1038/nature14066 PMID: 25600270

65. Granger CWJ. Investigating Causal Relations by Econometric Models and Cross-spectral Methods. Econometrica. 1969 Aug; 37(3):424.

66. Lynn CW, Holmes CM, Bialek W, Schwab DJ. Decomposing the local arrow of time in interacting systems. 2021 [cited 2022 Mar 31]; Available from: https://arxiv.org/abs/2112.14721.

67. Williams MA, Dang S, Kanwisher NG. Only some spatial patterns of fMRI response are read out in task performance. Nat Neurosci. 2007 Jun; 10(6):685–6. https://doi.org/10.1038/nn1900 PMID: 17486103

68. Ito T, Yang GR, Laurent P, Schultz DH, Cole MW. Constructing neural network models from brain data reveals representational transformations underlying adaptive behavior [Internet]. Neuroscience.; 2020 Dec [cited 2021 Jan 5]. Available from: http://biorxiv.org/lookup/doi/10.1101/2020.12.24.424353.

69. Reid AT, Headley DB, Mill RD, Sanchez-Romero R, Uddin LQ, Marinazzo D, et al. Advancing functional connectivity research from association to causation. Nat Neurosci. 2019; 22 (11):1751–60. https://doi.org/10.1038/s41593-019-0510-4 PMID: 31611705

70. Cole MW, Bassett DS, Power JD, Braver TS, Petersen SE. Intrinsic and Task-Evoked Network Architectures of the Human Brain. Neuron. 2014 Jul; 83(1):238–51. https://doi.org/10.1016/j.neuron.2014.05.014 PMID: 24991964

71. Krienen FM, Yeo BTT, Buckner RL. Reconfigurable task-dependent functional coupling modes cluster around a core functional architecture. Philos Trans R Soc B Biol Sci. 2014 Sep 1; 369 (1653):20130526–20130526. https://doi.org/10.1098/rstb.2013.0526 PMID: 25180304

72. Gates KM, Molenaar PCM, Hillary FG, Ram N, Rovine MJ. Automatic search for fMRI connectivity mapping: An alternative to Granger causality testing using formal equivalences among SEM path modeling, VAR, and unified SEM. Neuroimage. 2010 Apr; 50(3):1118–25. https://doi.org/10.1016/j.neuroimage.2009.12.117 PMID: 20060050

73. Liégeois R, Laumann TO, Snyder AZ, Zhou J, Yeo BTT. Interpreting temporal fluctuations in resting-state functional connectivity MRI. Neuroimage. 2017 Dec; 163:437–55. https://doi.org/10.1016/j.neuroimage.2017.09.012 PMID: 28916180

74. Mill RD, Bagic A, Bostan A, Schneider W, Cole MW. Empirical validation of directed functional connectivity. Neuroimage. 2016; 14 (146):275–87. https://doi.org/10.1016/j.neuroimage.2016.11.037 PMID: 27856312

75. Cybenko G. Approximation by superpositions of a sigmoidal function. Math Control Signals Syst. 1989 Dec; 2(4):303–14.

76. Corbetta M, Patel G, Shulman GL. The Reorienting System of the Human Brain: From Environment to Theory of Mind. Neuron. 2008 May; 58(3):306–24. https://doi.org/10.1016/j.neuron.2008.04.017 PMID: 18466742

77. Newbold DJ, Gordon EM, Laumann TO, Seider NA, Montez DF, Gross SJ, et al. Cingulo-Opercular Control Network Supports Disused Motor Circuits in Standby Mode [Internet]. Neuroscience.; 2020 Sep [cited 2020 Dec 23]. Available from: http://biorxiv.org/lookup/doi/10.1101/2020.09.03.275479.

78. Cocuzza CV, Ito T, Schultz D, Bassett DS, Cole MW. Flexible Coordinator and Switcher Hubs for Adaptive Task Control. J Neurosci. 2020 Sep 2; 40(36):6949–68. https://doi.org/10.1523/JNEUROSCI.2559-19.2020 PMID: 32732324

79. Cole MW, Reynolds JR, Power JD, Repovs G, Anticevic A, Braver TS. Multi-task connectivity reveals flexible hubs for adaptive task control. Nat Neurosci. 2013 Jul 28; 16(9):1348–55. https://doi.org/10.1038/nn.3470 PMID: 23892552

80. Megevand P, Spinelli L, Genetti M, Brodbeck V, Momjian S, Schaller K, et al. Electric source imaging of interictal activity accurately localises the seizure onset zone. J Neurol Neurosurg Psychiatry. 2014 Jan 1; 85(1):38–43. https://doi.org/10.1136/jnnp-2013-305515 PMID: 23899624

81. Ji JL, Spronk M, Kulkarni K, Repovš G, Anticevic A, Cole MW. Mapping the human brain's cortical-subcortical functional network organization. Neuroimage. 2019 Jan; 185:35–57. https://doi.org/10.1016/j.neuroimage.2018.10.006 PMID: 30291974

82. King M, Hernandez-Castillo CR, Poldrack RA, Ivry RB, Diedrichsen J. Functional boundaries in the human cerebellum revealed by a multi-domain task battery. Nat Neurosci. 2019 Aug; 22(8):1371–8. https://doi.org/10.1038/s41593-019-0436-x PMID: 31285616

83. Sadaghiani S, Dombert PL, Løvstad M, Funderud I, Meling TR, Endestad T, et al. Lesions to the Fronto-Parietal Network Impact Alpha-Band Phase Synchrony and Cognitive Control. Cereb Cortex [Internet] 2018 Dec 7 [cited 2021 Jan 22]; Available from: https://academic.oup.com/cercor/advance-article/doi/10.1093/cercor/bhy296/5232534.

84. Huang YZ, Edwards MJ, Rounis E, Bhatia KP, Rothwell JC. Theta Burst Stimulation of the Human Motor Cortex. Neuron. 2005 Jan; 45(2):201–6. https://doi.org/10.1016/j.neuron.2004.12.033 PMID: 15664172

85. Polanía R, Nitsche MA, Korman C, Batsikadze G, Paulus W. The Importance of Timing in Segregated Theta Phase-Coupling for Cognitive Performance. Curr Biol. 2012 Jul; 22(14):1314–8. https://doi.org/10.1016/j.cub.2012.05.021 PMID: 22683259

86. Gordon EM, Laumann TO, Gilmore AW, Newbold DJ, Greene DJ, Berg JJ, et al. Precision Functional Mapping of Individual Human Brains. Neuron. 2017 Aug; 95(4):791–807.e7. https://doi.org/10.1016/j.neuron.2017.07.011 PMID: 28757305

87. Gratton C, Laumann TO, Nielsen AN, Greene DJ, Gordon EM, Gilmore AW, et al. Functional Brain Networks Are Dominated by Stable Group and Individual Factors, Not Cognitive or Daily Variation Neuron. 2018 Apr; 98(2):439–452.e5.

88. Woo CW, Chang LJ, Lindquist MA, Wager TD. Building better biomarkers: brain models in translational neuroimaging. Nat Neurosci. 2017 Feb 23; 20(3):365–77. https://doi.org/10.1038/nn.4478 PMID: 28230847

89. de Cheveigné A, Nelken I. Filters: When, Why, and How (Not) to Use Them. Neuron. 2019 Apr; 102 (2):280–93. https://doi.org/10.1016/j.neuron.2019.02.039 PMID: 30998899

90. Rousselet GA. Does Filtering Preclude Us from Studying ERP Time-Courses? Front Psychol [Internet] 2012 [cited 2020 Oct 7]; 3. Available from: http://journal.frontiersin.org/article/10.3389/fpsyg.2012.00131/abstract. https://doi.org/10.3389/fpsyg.2012.00131 PMID: 22586415

91. Widmann A, Schröger E. Filter Effects and Filter Artifacts in the Analysis of Electrophysiological Data. Front Psychol [Internet]. 2012 [cited 2020 Oct 7]; 3. Available from: http://journal.frontiersin.org/article/10.3389/fpsyg.2012.00233/abstract. https://doi.org/10.3389/fpsyg.2012.00233 PMID: 22787453

92. Widmann A, Schröger E, Maess B. Digital filter design for electrophysiological data–a practical approach. J Neurosci Methods. 2015 Jul; 250:34–46. https://doi.org/10.1016/j.jneumeth.2014.08.002 PMID: 25128257

93. Luck SJ. An introduction to the event-related potential technique. Cambridge, Mass: MIT Press; 2005. 374 p. (Cognitive neuroscience).

94. Oostenveld R, Fries P, Maris E, Schoffelen JM. FieldTrip: Open Source Software for Advanced Analysis of MEG, EEG, and Invasive Electrophysiological Data. Comput Intell Neurosci. 2011; 2011:1–9.

95. Jung TP, Makeig S, McKeown MJ, Bell AJ, Lee TW, Sejnowski TJ. Imaging brain dynamics using independent component analysis. Proc IEEE. 2001 Jul; 89(7):1107–22. https://doi.org/10.1109/5.939827 PMID: 20824156

96. Delorme A, Makeig S. EEGLAB: an open source toolbox for analysis of single-trial EEG dynamics including independent component analysis. J Neurosci Methods. 2004 Mar; 134(1):9–21. https://doi.org/10.1016/j.jneumeth.2003.10.009 PMID: 15102499

97. Chaumon M, Bishop DVM, Busch NA. A practical guide to the selection of independent components of the electroencephalogram for artifact correction. J Neurosci Methods. 2015 Jul; 250:47–63. https://doi.org/10.1016/j.jneumeth.2015.02.025 PMID: 25791012

98. Pontifex MB, Miskovic V, Laszlo S. Evaluating the efficacy of fully automated approaches for the selection of eyeblink ICA components: Eyeblink component identification. Psychophysiology. 2017 May; 54 (5):780–91. https://doi.org/10.1111/psyp.12827 PMID: 28191627

99. Goncharova II, McFarland DJ, Vaughan TM, Wolpaw JR. EMG contamination of EEG: spectral and topographical characteristics. Clin Neurophysiol. 2003 Sep; 114(9):1580–93. https://doi.org/10.1016/s1388-2457(03)00093-2 PMID: 12948787

100. Pernet C, Garrido MI, Gramfort A, Maurits N, Michel CM, Pang E, et al. Issues and recommendations from the OHBM COBIDAS MEEG committee for reproducible EEG and MEG research. Nat Neurosci [Internet]. 2020 Sep 21 [cited 2020 Oct 7]; Available from: http://www.nature.com/articles/s41593-020-00709-0. https://doi.org/10.1038/s41593-020-00709-0 PMID: 32958924

101. Michel CM, Brunet D. EEG Source Imaging: A Practical Review of the Analysis Steps. Front Neurol [Internet]. 2019 Apr 4 [cited 2020 Oct 7]; 10. Available from: https://www.frontiersin.org/article/10.3389/fneur.2019.00325/full. https://doi.org/10.3389/fneur.2019.00325 PMID: 31019487

102. Gordon EM, Laumann TO, Adeyemo B, Huckins JF, Kelley WM, Petersen SE. Generation and Evaluation of a Cortical Area Parcellation from Resting-State Correlations. Cereb Cortex. 2016 Jan; 26 (1):288–303. https://doi.org/10.1093/cercor/bhu239 PMID: 25316338

103. Glasser MF, Coalson TS, Robinson EC, Hacker CD, Harwell J, Yacoub E, et al. A multi-modal parcellation of human cerebral cortex. Nature. 2016 Jul 20; 536(7615):171–8. https://doi.org/10.1038/nature18933 PMID: 27437579

104. Stafford JM, Jarrett BR, Miranda-Dominguez O, Mills BD, Cain N, Mihalas S, et al. Large-scale topology and the default mode network in the mouse connectome. Proc Natl Acad Sci. 2014 Dec 30; 111 (52):18745–50. https://doi.org/10.1073/pnas.1404346111 PMID: 25512496

105. Wang Z, Chen LM, Négyessy L, Friedman RM, Mishra A, Gore JC, et al. The Relationship of Anatomical and Functional Connectivity to Resting-State Connectivity in Primate Somatosensory Cortex. Neuron. 2013 Jun; 78(6):1116–26. https://doi.org/10.1016/j.neuron.2013.04.023 PMID: 23791200

106. Chang CC, Lin CJ. LIBSVM: A library for support vector machines. ACM Trans Intell Syst Technol. 2011 Apr; 2(3):1–27.

107. Oosterhof NN, Connolly AC, Haxby JV. CoSMoMVPA: Multi-Modal Multivariate Pattern Analysis of Neuroimaging Data in Matlab/GNU Octave. Front Neuroinformatics [Internet]. 2016 Jul 22 [cited 2020 Oct 8]; 10. Available from: http://journal.frontiersin.org/Article/10.3389/fninf.2016.00027/abstract. https://doi.org/10.3389/fninf.2016.00027 PMID: 27499741

108. Poldrack RA, Huckins G, Varoquaux G. Establishment of Best Practices for Evidence for Prediction: A Review. JAMA Psychiatry [Internet]. 2019 Nov 27 [cited 2020 Feb 9]; Available from: https://jamanetwork.com/journals/jamapsychiatry/fullarticle/2756204.

109. Muraskin J, Dodhia S, Lieberman G, Garcia JO, Verstynen T, Vettel JM, et al. Brain dynamics of post-task resting state are influenced by expertise: Insights from baseball players. Hum Brain Mapp. 2016 Dec; 37(12):4454–71. https://doi.org/10.1002/hbm.23321 PMID: 27448098

110. Cole MW, Ito T, Schultz D, Mill R, Chen R, Cocuzza C. Task activations produce spurious but systematic inflation of task functional connectivity estimates. Neuroimage. 2019 Apr; 189:1–18. https://doi.org/10.1016/j.neuroimage.2018.12.054 PMID: 30597260

111. Mitra A, Raichle ME. How networks communicate: propagation patterns in spontaneous brain activity. Philos Trans R Soc B Biol Sci 2016 Oct 5; 371(1705):20150546. https://doi.org/10.1098/rstb.2015.0546 PMID: 27574315

112. Kim J, Zhu W, Chang L, Bentler PM, Ernst T. Unified structural equation modeling approach for the analysis of multisubject, multivariate functional MRI data. Hum Brain Mapp. 2007 Feb; 28(2):85–93. https://doi.org/10.1002/hbm.20259 PMID: 16718669

113. Hutchison RM, Womelsdorf T, Allen EA, Bandettini PA, Calhoun VD, Corbetta M, et al. Dynamic functional connectivity: Promise, issues, and interpretations. Neuroimage. 2013 Oct; 80:360–78. https://doi.org/10.1016/j.neuroimage.2013.05.079 PMID: 23707587

114. Laumann TO, Snyder AZ, Mitra A, Gordon EM, Gratton C, Adeyemo B, et al. On the Stability of BOLD fMRI Correlations. Cereb Cortex [Internet]. 2016 Sep 2 [cited 2017 Jan 26]; Available from: http://cercor.oxfordjournals.org/cgi/doi/10.1093/cercor/bhw265.

115. Sanchez-Romero R, Cole MW. Combining Multiple Functional Connectivity Methods to Improve Causal Inferences. J Cogn Neurosci. 2020 May 19;1–15. https://doi.org/10.1162/jocn_a_01580 PMID: 32427070

116. Stevenson IH. Omitted Variable Bias in GLMs of Neural Spiking Activity. Neural Comput. 2018 Dec; 30(12):3227–58. https://doi.org/10.1162/neco_a_01138 PMID: 30314428

117. Geweke J. Measurement of Linear Dependence and Feedback between Multiple Time Series. J Am Stat Assoc. 1982 Jun; 77(378):304–13.

118. Cheung BLP, Riedner BA, Tononi G, Van Veen B. Estimation of Cortical Connectivity From EEG Using State-Space Models. IEEE Trans Biomed Eng. 2010 Sep; 57(9):2122–34. https://doi.org/10.1109/TBME.2010.2050319 PMID: 20501341

119. Roebroeck A, Formisano E, Goebel R. The identification of interacting networks in the brain using fMRI: Model selection, causality and deconvolution. Neuroimage. 2011 Sep 15; 58(2):296–302. https://doi.org/10.1016/j.neuroimage.2009.09.036 PMID: 19786106

120. Kucyi A, Schrouff J, Bickel S, Foster BL, Shine JM, Parvizi J. Intracranial Electrophysiology Reveals Reproducible Intrinsic Functional Connectivity within Human Brain Networks. J Neurosci. 2018 Apr 25; 38(17):4230–42. https://doi.org/10.1523/JNEUROSCI.0217-18.2018 PMID: 29626167

121. Vincent JL, Patel GH, Fox MD, Snyder AZ, Baker JT, Van Essen DC, et al. Intrinsic functional architecture in the anaesthetized monkey brain. Nature. 2007 May; 447(7140):83–6. https://doi.org/10.1038/nature05758 PMID: 17476267

122. Crowe DA, Goodwin SJ, Blackman RK, Sakellaridi S, Sponheim SR, MacDonald AW, et al. Prefrontal neurons transmit signals to parietal neurons that reflect executive control of cognition. Nat Neurosci. 2013 Oct; 16(10):1484–91. https://doi.org/10.1038/nn.3509 PMID: 23995071

123. Murray JD, Bernacchia A, Freedman DJ, Romo R, Wallis JD, Cai X, et al. A hierarchy of intrinsic timescales across primate cortex. Nat Neurosci. 2014 Dec; 17(12):1661–3. https://doi.org/10.1038/nn.3862 PMID: 25383900

124. Cole MW, Bagic A, Kass R, Schneider W. Prefrontal Dynamics Underlying Rapid Instructed Task Learning Reverse with Practice. J Neurosci. 2010 Oct 20; 30(42):14245–54. https://doi.org/10.1523/JNEUROSCI.1662-10.2010 PMID: 20962245

125. Cerqueira V, Torgo L, Mozetic I. Evaluating time series forecasting models: An empirical study on performance estimation methods. ArXiv190511744 Cs Stat [Internet]. 2019 May 28 [cited 2020 Oct 13]; Available from: http://arxiv.org/abs/1905.11744.

126. Nolte G, Bai O, Wheaton L, Mari Z, Vorbach S, Hallett M. Identifying true brain interaction from EEG data using the imaginary part of coherency. Clin Neurophysiol. 2004 Oct; 115(10):2292–307. https://doi.org/10.1016/j.clinph.2004.04.029 PMID: 15351371

127. Diedrichsen J, Kriegeskorte N. Representational models: A common framework for understanding encoding, pattern-component, and representational-similarity analysis. Cichy R, editor. PLoS Comput Biol. 2017 Apr 24; 13(4):e1005508. https://doi.org/10.1371/journal.pcbi.1005508 PMID: 28437426

128. Mur M, Bandettini PA, Kriegeskorte N. Revealing representational content with pattern-information fMRI—an introductory guide. Soc Cogn Affect Neurosci. 2009 Mar; 4(1):101–9. https://doi.org/10.1093/scan/nsn044 PMID: 19151374